



TELECOMMUNICATION
ENGINEERING



UNIVERSITY
of
TWENTE

University of Twente
Department of Electrical Engineering
Chair for Telecommunication Engineering

Performance Evaluation of Frequency Modulation and Slope Detection in Analog Optical Links

by

R.B. Timens

May 28, 2009

Master thesis

Executed from 01-04-2008 to 27-03-2009

Supervisor: prof.dr.ir. F.B.J. Leferink

Advisors: dr.ir. C.G.H. Roeloffzen

ir. D.A.I. Marpaung

Summary

One unsolved challenge in the application of analog optical links is the limited dynamic range. It is desirable to have a scheme which offers low noise and high linearity. In other words, it is required to have a scheme employing Class-B operation in analog optical links. In a Class-B optical link all received optical power contributes to the radio frequency (RF)-signal power. Since the noise is dependent on the average optical power, the noise in a Class-B optical link depends on the signal power.

A good candidate for the Class-B scheme is the combination of frequency modulation and slope detection. The scheme consists of a directly modulated laser and an integrated optical filter. The directly modulated laser generates the frequency modulated signal. The optical filter converts the signal into two intensity modulated signals. At the receiver end, these signals are detected by a balanced photodetector. It restores the original modulating signal.

The filter performing the slope detection consists of two-coupler rings. It is designed in such a way, that the conversion from frequency modulation to intensity modulation will yield two optical signals that comprise the complementary half-wave rectified versions of the original modulating signal. This half-wave rectification is the key element for realizing the Class-B operation in analog optical links.

The report gives an overview of the filter design. Furthermore, the feasibility of frequency modulation by the laser and the feasibility of half-wave rectification based on optical frequency modulation are experimentally shown.

Contents

| | |
|---|------------|
| Summary | iii |
| List of Abbreviations and Symbols | vii |
| 1 Introduction | 1 |
| 1.1 Problem Description | 1 |
| 1.2 Assignment Description | 4 |
| 1.3 Report Outline | 4 |
| 2 General Analog Optical Link Performance | 7 |
| 2.1 AOL Scheme | 7 |
| 2.2 Link Gain | 8 |
| 2.3 Noise | 8 |
| 2.4 Distortion | 10 |
| 2.5 Spurious Free Dynamic Range (SFDR) | 12 |
| 2.6 Numerical Example | 14 |
| 3 Ideal Class-B AOL | 17 |
| 3.1 Principle of Class-B in AOL | 17 |
| 3.2 Noise | 17 |
| 3.3 Distortion | 20 |
| 3.4 Dynamic Range | 20 |
| 4 Frequency Modulation-Slope Detection Analog Optical Link | 23 |
| 4.1 Frequency Modulation-Slope Detection Scheme | 23 |
| 5 Filter Design and Simulation | 25 |
| 5.1 Design Requirements | 25 |
| 5.2 Digital Filter Design Approach | 26 |
| 5.3 Available Components for Design | 27 |
| 5.3.1 Directional Coupler | 28 |
| 5.3.2 Mach-Zehnder Interferometer | 28 |

| | | |
|----------|---|-----------|
| 5.3.3 | Ring Resonator | 30 |
| 5.4 | Slope Detector Design | 33 |
| 5.4.1 | DC Power Divider and Two MZIs | 33 |
| 5.4.2 | DC Power Divider and Two Ring-Resonators | 35 |
| 5.4.3 | Three Ring-Resonators | 37 |
| 5.4.4 | Five Ring-Resonators | 39 |
| 6 | Measurements | 43 |
| 6.1 | Semiconductor Laser Diode P-I Curve | 43 |
| 6.1.1 | Measurement Setup | 43 |
| 6.1.2 | Measurement Results | 44 |
| 6.2 | Temperature and Current Dependences of SLD Wavelength | 46 |
| 6.2.1 | Measurement Setup | 46 |
| 6.2.2 | Measurement Results | 46 |
| 6.3 | DWDM Filter Transfer and SLD FM Response | 48 |
| 6.3.1 | Measurement Setup | 48 |
| 6.3.2 | Measurement Results | 50 |
| 7 | Conclusion and Recommendations | 63 |
| A | SFDR, OIP and Noise Level | 67 |
| B | Tables | 69 |

List of Abbreviations and Symbols

Abbreviations

| | |
|-------------|--|
| AOL | analog optical link |
| BMD | balanced modulation and detection |
| BPD | balanced photodetector |
| CW | continuous wave |
| DC | directional coupler |
| DR | dynamic range |
| DWDM | dense wavelength division multiplexing |
| EAM | electroabsorption modulator |
| EMI | electromagnetic interference |
| FIR | finite impulse response |
| FM | frequency modulation |
| FSR | free spectral range |
| HWR | half-wave rectification |
| IM | intensity modulation |
| IMDD | intensity modulation direct detection |
| MZI | Mach-Zehnder interferometer |
| MZM | Mach-Zehnder modulator |
| NA | network analyzer |
| NF | noise figure |

| | |
|-------------|-----------------------------|
| OIP | output intercept point |
| OSA | optical spectrum analyzer |
| RF | radio frequency |
| RIN | relative intensity noise |
| RMS | root mean square |
| SDR | signal-to-distortion ratio |
| SFDR | spurious free dynamic range |
| SLD | semiconductor laser diode |
| SNR | signal-to-noise ratio |
| VOA | variable optical attenuator |

Symbols

| | |
|-------------------------|---|
| A | amplitude |
| A_i | amplitude |
| a_i | power series coefficient |
| BW | bandwidth in dB |
| bw | bandwidth in Hz |
| c | speed of light |
| Δ_f | maximum frequency deviation |
| ΔL_{MZI} | relative length difference MZI branches |
| Δ_m | maximum RF-current |
| DR_2 | second-order dynamic range |
| DR_3 | third-order dynamic range |
| f_c | carrier frequency |
| FSR_{MZI} | MZI free spectral range |
| FSR_{ring} | ring free spectral range |

| | |
|--------------------------|---|
| G_{link} | link gain |
| $G_{\text{link,CB}}$ | link gain Class-B optical link |
| $G_{\text{link,IMDD}}$ | link gain IMDD optical link |
| I_1 | laser bias current |
| i_1 | laser RF-current amplitude |
| I_{ph} | detected photocurrent |
| I_t | laser threshold current |
| κ_{DC} | DC power coupling coefficient |
| $\kappa_{\text{MZI},1}$ | MZI power coupling coefficient 1 |
| $\kappa_{\text{MZI},2}$ | MZI power coupling coefficient 2 |
| $\kappa_{\text{ring},1}$ | ring power coupling coefficient 1 |
| $\kappa_{\text{ring},2}$ | ring power coupling coefficient 2 |
| L_{MZI} | common path length MZI branches |
| l_{ring} | ring round trip loss |
| L_U | unit length |
| n | refractive index |
| N_{out} | output noise power |
| OIP_n | power level n-th-order output intercept point |
| OIP_2 | power level second-order output intercept point |
| OIP_3 | power level third-order output intercept point |
| Φ_{DC} | transfer matrix DC |
| P_F | fundamental power |
| P_{IM_2} | second-order intermodulation power |
| P_{IM_3} | third-order intermodulation power |
| P_{in} | RF-input power |

| | |
|----------------------|---|
| p_{\max} | maximum magnitude of fundamental |
| p_{\min} | minimum magnitude of fundamental |
| Φ_{MZI} | transfer matrix MZI |
| ϕ_{MZI} | MZI phase |
| $P_{\text{n,total}}$ | total noise power |
| P_{op} | optical power |
| $P_{\text{op,CB}}$ | optical power per branch in Class-B optical link |
| $P_{\text{op,IMDD}}$ | optical power IMDD optical link |
| P_{out} | RF-output power |
| P_{RIN} | RIN power |
| ϕ_{ring} | ring round trip phase |
| Φ_{ring} | transfer matrix ring |
| P_{shot} | shot noise power |
| P_{therm} | thermal noise power |
| R_{in} | input resistance |
| RIN_{laser} | laser RIN power spectral density |
| R_{load} | load resistance |
| R_{pd} | photodetector responsivity |
| R_{ring} | ring radius ring resonator |
| $SFDR_n$ | n-th-order intermodulation free spurious free dynamic range |
| $SFDR_2$ | second-order intermodulation free spurious free dynamic range |
| $SFDR_3$ | third-order intermodulation free spurious free dynamic range |
| s_1 | laser slope efficiency |
| T | absolute temperature |
| t | time |

| | |
|------------|-----------------------------|
| T_U | unit delay |
| ω | angular frequency |
| ω_i | angular frequency |
| $x(t)$ | input function of time t |
| $y(t)$ | output function of time t |

Introduction

1.1 Problem Description

Analog optical links (AOLs) are used in a wide variety of applications for RF and microwave signals distribution. In many applications, such as antenna beam forming and phased array systems, the links are required to convey signals over a large span of power levels, posing stringent requirements on their signal-to-noise ratio (SNR) and linearity [1]. Noise limits the minimum detectable RF-signal power while distortion limits the maximum RF-signal power, resulting in a limited dynamic range (DR).

Therefore, it is desired to have a scheme which offers low noise and is sufficiently linear. Several approaches have been done to obtain this scheme by using the simple concept of direct detecting an intensity modulated signal or intensity modulation direct detection (IMDD). The non-physical ideal response for intensity modulation (IM) is given in Figure 1.1. Note that negative optical power does not exist. In this figure the modulation signal is a current or a voltage, depending on the implementation. The shown response is ideal, since there is no optical power when the signal is zero. Moreover, the curve is linear. These two properties are essential for obtaining high DR as will become clear later on. As far we know, however, the ideal response is never approached to a satisfying degree. We can find the reason for this in [3], where it is argued that the conventional IMDD links do not meet the two aforementioned requirements.

For example, consider the case of direct modulation of a semiconductor laser diode (SLD), and the two cases of external modulation of a continuous wave (CW) laser by a Mach-Zehnder modulator (MZM) and an electroabsorption modulator (EAM). The corresponding responses are shown in Figure 1.2. For the purpose of linear operation, the laser and modulators are biased as indicated by the dot, resulting in large average optical power. Detection of large optical power will result in large noise power, since the dominant noise sources, RIN and shot noise, are increasing with the optical power [5]. This, in turn, will limit the link DR [2]. For the purpose of operation at low average

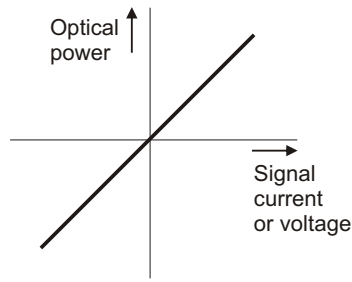


Figure 1.1: Non-physical ideal response for IM

optical power, the laser and modulators are biased as indicated by the square, resulting in large nonlinearities. This, in turn, will also limit the link DR [2].

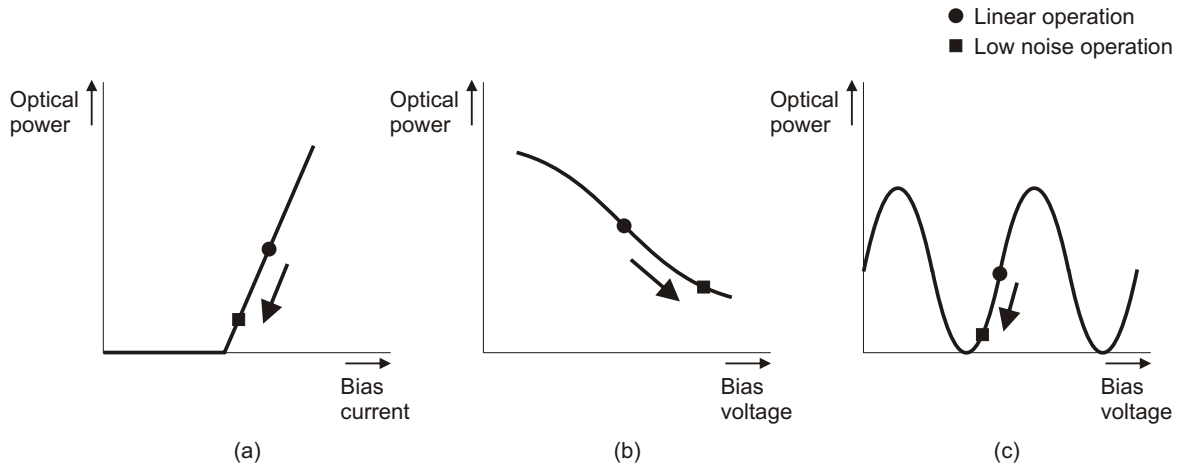


Figure 1.2: Biasing of an SLD (a), an EAM (b) and an MZM (c)

Figure 1.3 illustrates the limitations in DR for the case of direct modulation in more detail. As shown in Figure 1.3 (a) low biasing results in a low average optical power and therefore in a low noise power, but also in clipping of large signals. Higher biasing avoids the signal clipping, but also results in a larger average optical power and thus a larger noise power. This larger noise power dominates over small signals, as is shown in Figure 1.3 (b).

In order to decrease the large noise power without increasing the nonlinearities, one could attempt to use a balanced transmitter in which two SLDs are biased around threshold. In this way, one can theoretically obtain the ideal response of Figure 1.1. However, as is shown in [6], biasing a laser near threshold point leads to nonlinearities in the laser and relative intensity noise (RIN) enhancement, which limits the achievable DR of this so called balanced modulation and detection (BMD) link.

The work of [6] uses the BMD scheme in an attempt to obtain a link in which all received optical power linearly contributes to the RF-signal power. In other words, it is tried to obtain a link which operates without a dc-bias. The ideal case of such a

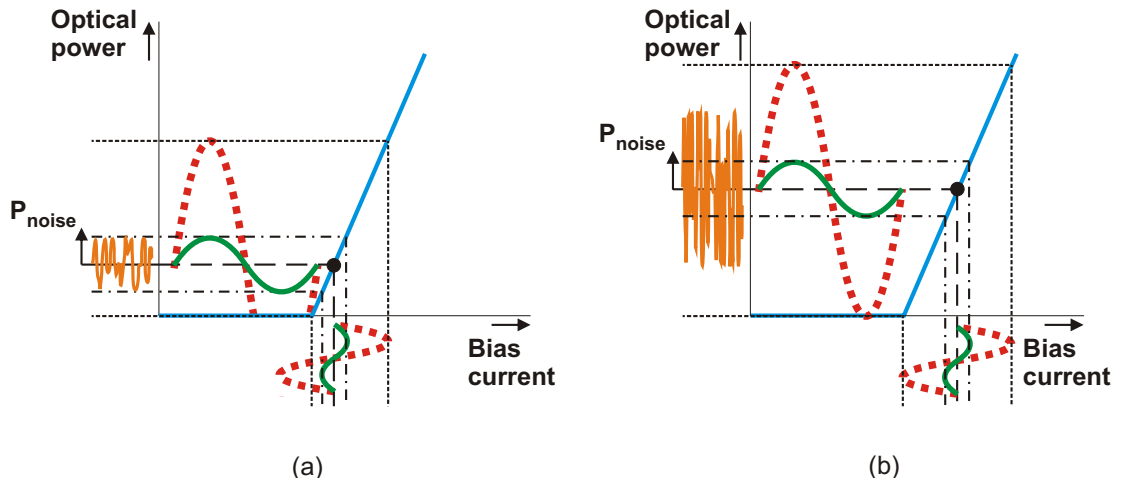


Figure 1.3: Biasing of an intensity modulated SLD: low biasing results in clipping of large signals (a), but high biasing results in a large optical power and therefore a large noise power (b).

link operation is known as Class-B operation [3]. To realize the Class-B optical link, several methods have been proposed [3], [6]. But, all these attempts have resulted in limited improvement due to an increase in nonlinearities or noise [3].

In this report, we propose a scheme to realize the Class-B optical link. We use an integrated optical ring-resonator based slope detector (or frequency discriminator) to realize the ideal response in Figure 1.1. The scheme in Figure 1.4 shows the frequency modulation-slope detection analog optical link (AOL), in which the electrical parts and optical parts are explicitly indicated. It is widely known that a direct modulated

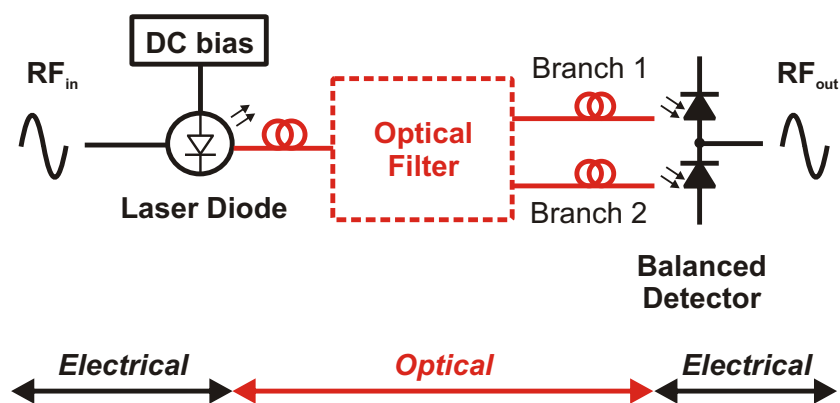


Figure 1.4: The frequency modulation (FM)-slope detection AOL

SLD exhibits variation in its intensity as well as in its frequency. This FM is known as the frequency chirping. In this scheme, the frequency chirp is used to carry the information. By means of optical filtering, the FM is subsequently converted to IM.

The filter responses are chosen such that the resulting intensity modulated signals are complementary half-wave rectified versions of the modulating RF-signal. These optical signals are detected by a balanced photodetector (BPD) in the receiving side. The desired filter responses are shown in Figure 1.5 and subtraction of the two individual responses results in a straight line, which is required for slope detection. The corre-

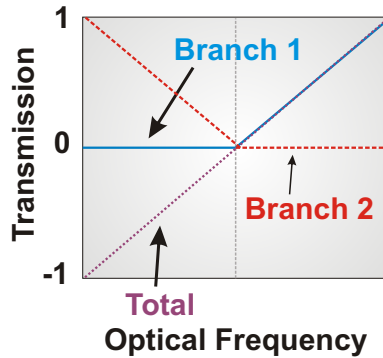


Figure 1.5: Optical filter responses

sponding half-wave rectification (HWR) suppresses the dc optical carrier which is the main contributor for the total RF noise power in AOLs. The reduction in noise power by this optical carrier suppression will lead to DR enhancement.

1.2 Assignment Description

The main goal of the project is to design the integrated optical slope detector and to demonstrate the FM-slope detection scheme. The following tasks are carried out during the project:

1. Investigate the feasibility of optical FM in SLDs.
2. Design of the optical filter according to the desired response of Figure 1.5.
3. Investigate the feasibility of HWR based on optical FM.

1.3 Report Outline

In Chapter 2 the general AOL scheme and its performance are discussed. In Chapter 3 the characteristics of the ideal Class-B link are discussed. This discussion evaluates the ideal Class-B optical link performance using the conventional IMDD link as a benchmark. In Chapter 4 the FM-slope detection AOL is described and attention will be paid on how Class-B operation is obtained using this link. This discussion is the

starting point for the slope detector design on which Chapter 5 is devoted. For this design, simulations in LabVIEW 8.5 are carried out. Since it is not possible to fabricate the filter in the project, existing DWDM-filters are used for the measurements. In this way, the concept or principal can be verified. The results of these measurements are discussed in Chapter 6. The report closes with the conclusion in Chapter 7.

General Analog Optical Link Performance

In this chapter the analog optical link (AOL) is introduced. First, the general scheme and its advantages are discussed. Next, the discussion continues with the problems related to AOLs. In this discussion, the terms link gain, relative intensity noise (RIN), shot noise, thermal noise, harmonic distortion, intermodulation distortion and spurious free dynamic range (SFDR) are defined.

2.1 AOL Scheme

AOLs are used in a wide variety of applications for RF and microwave signals distribution, due to the following advantages over coaxial cables:

- low propagation loss
- wide bandwidth
- immunity for electromagnetic interference (EMI)
- small size
- light weight.

The general scheme of an AOL is shown in Figure 2.1. It consists of an electro-to-optical converter (modulation device) and an optical-to-electrical converter (optical detector). At the input of the link, the RF-signal is converted to the optical domain by the modulation device. At the output of the link, the signal is back-converted to the RF domain by the optical detector.

The conversion efficiency in the modulation device is called slope efficiency. Depending on the implementation, it is defined as the ratio of the variation in optical power over the corresponding variation in current (in W/A) or voltage (in W/V). The



Figure 2.1: General AOL-scheme

conversion efficiency in the optical detector is called responsivity. It is defined as the ratio of the variation in current over the corresponding variation in detected optical power (in A/W). However, the conversions are inefficient. Practical values for the SLD slope efficiency are between 0.015 and 0.3 W/A, and for the photodiode responsivity are between 0.7 and 1.0 A/W [5]. Furthermore, the conversions are accompanied by noise and distortion [5]. This will, in turn, degrade the performance of an AOL.

2.2 Link Gain

The link gain, G_{link} , can be defined as the ratio of RF-output and -input powers as follows:

$$G_{link} = \frac{P_{out}}{P_{in}} \quad (2.1a)$$

or, in decibels it can be expressed as:

$$G_{link} \text{ (dB)} = P_{out} \text{ (dBm)} - P_{in} \text{ (dBm)} \quad (2.1b)$$

In Equation (2.1) P_{in} denotes the RF-input power and P_{out} the RF-output power of the link. Because of the inefficient conversions in the modulation device and optical detector, the output power of the AOL is smaller than the input power. This results in a link gain value which is smaller than 1. In other words, the optical link can be considered as a lossy component.

2.3 Noise

Three noise sources are contributing to the link noise. The first one is relative intensity noise (RIN) and finds its origin in the laser. Spontaneous emission is needed to initialize the laser mechanism (stimulated emission) in an SLD. However, it is still present when an SLD is in lasing mode and therefore contributes an incoherent part to the laser output field. Especially around threshold current, the spontaneous emitted power relative to the stimulated emitted power is large.

The laser RIN-power spectral density, RIN_{laser} , is defined as the variance of the spontaneous emitted power relative to the square of the total average optical power as shown in Equation (2.2) [5]. The laser RIN-power spectral density is unitless.

$$RIN_{\text{laser}} = \frac{\langle (P_{\text{op}} - \langle P_{\text{op}} \rangle)^2 \rangle}{\langle P_{\text{op}} \rangle^2} = \frac{\langle p_{\text{RIN}}^2 \rangle}{\langle P_{\text{op}} \rangle^2} \quad (2.2)$$

The spontaneous emitted power or incoherent part of the output field gives rise to instantaneous intensity fluctuations, and detection of these fluctuations results in intensity noise. The associated RIN power per unit electrical bandwidth, P_{RIN} , is described as:

$$P_{\text{RIN}} \text{ (W/Hz)} = RIN_{\text{laser}} \cdot \langle I_{\text{ph}} \rangle^2 \cdot R_{\text{load}} \quad (2.3)$$

In Equation (2.3), RIN_{laser} denotes the laser RIN-power spectral density (in 1/Hz), I_{ph} denotes the detected photocurrent (in A) and R_{load} denotes the load resistance (in Ω). I_{ph} depends on the photodetector responsivity, R_{pd} (in A/W), and optical power, P_{op} (in W), as follows:

$$I_{\text{ph}} \text{ (A)} = R_{\text{pd}} \cdot P_{\text{op}} \quad (2.4)$$

The second noise source is the shot noise which finds its origin in the generation of photocurrents arising from a series of independent random events. Mainly, it is driven by the random arrival of photons on the photodetector [5]. This results in an instantaneous current, which is not constant, although the average current is constant. The shot noise power, P_{shot} , is described as [5]:

$$P_{\text{shot}} \text{ (W/Hz)} = 2 \cdot e \cdot \langle I_{\text{ph}} \rangle \cdot R_{\text{load}} \quad (2.5)$$

The last noise source is the thermal noise and also finds its origin in the detector. The thermal noise is the result of thermal induced random movements of carriers giving rise to a nonzero instantaneous current, with zero average. Assuming impedance matching, the transferred thermal noise power is described as:

$$P_{\text{therm}} \text{ (W/Hz)} = k \cdot T \quad (2.6)$$

In Equation (2.6), k denotes Boltzmann's constant (in J/K) and T denotes the absolute temperature (in K). Unlike the RIN and shot noise power, the thermal noise power is independent of the optical power.

The total noise, $P_{\text{n,total}}$, in the AOL is the sum of Equations (2.3), (2.5) and (2.6):

$$P_{\text{n,total}} \text{ (W/Hz)} = P_{\text{RIN}} + P_{\text{shot}} + P_{\text{therm}} \quad (2.7a)$$

or, in decibels it can be expressed as:

$$P_{\text{n,total}} \text{ (dBm/Hz)} = 10 \log_{10} \left(\frac{P_{\text{RIN}} + P_{\text{shot}} + P_{\text{therm}}}{0.001} \right) \quad (2.7b)$$

2.4 Distortion

The nonlinearities in the modulation device and the optical detector result in distortion. To evaluate the nonlinear distortion, the transfer characteristic is mathematically expressed by writing the output $y(t)$ as a power series of the input $x(t)$:

$$y(t) = a_1x(t) + a_2x^2(t) + a_3x^3(t) + \dots \quad (2.8)$$

It is assumed that only the second- and third-order nonlinearities are of concern and as a result the fourth and higher order terms of Equation (2.8) are ignored. Consider a single sinusoidal wave at the input:

$$x(t) = A \cos(\omega t) \quad (2.9)$$

Harmonic distortion spectral components will then arise at the output at angular frequencies 0 , ω , 2ω and 3ω . Next, consider a two tone signal with the closely spaced tones ω_1 and ω_2 at the input:

$$x(t) = A_1 \cos(\omega_1 t) + A_2 \cos(\omega_2 t) \quad (2.10)$$

Now not only harmonic distortion, but also intermodulation distortion arises with spectral components at the sum and difference frequencies of the two tone signal, i.e. at $\omega_1 \pm \omega_2$, $2\omega_1 \pm \omega_2$ and $\omega_1 \pm 2\omega_2$. Table 2.1 gives an overview of the two types of distortion up to the third-order, with corresponding frequency and amplitude.

Table 2.1: Overview distortion components

| | Order | Angular frequency | Amplitude |
|-------------|--------------|--|---|
| Single tone | Dc | 0 | $\frac{1}{2}a_2A$ |
| | Fundamental | ω | $a_1A + \frac{3}{4}a_3A^3$ |
| | Second-order | 2ω | $\frac{1}{2}a_2A^2$ |
| | Third-order | 3ω | $\frac{1}{4}a_3A^3$ |
| Two tone | Dc | 0 | $\frac{1}{2}a_2A_1^2 + \frac{1}{2}a_2A_2^2$ |
| | Fundamental | ω_1, ω_2 | $a_1A_1 + \frac{3}{2}a_3A_1A_2^2 + \frac{3}{4}a_3A_1^3,$ $a_1A_2 + \frac{3}{2}a_3A_1^2A_2 + \frac{3}{4}a_3A_2^3$ |
| | Second-order | $\omega_1 + \omega_2, \omega_1 - \omega_2$ | $a_2A_1A_2, a_2A_1A_2$ |
| | | $2\omega_1, 2\omega_2$ | $\frac{1}{2}a_2A_1^2, \frac{1}{2}a_2A_2^2$ |
| | Third-order | $2\omega_1 + \omega_2, 2\omega_1 - \omega_2$ | $\frac{3}{4}a_3A_1^2A_2, \frac{3}{4}a_3A_1^2A_2$ |
| | | $\omega_1 + 2\omega_2, \omega_1 - 2\omega_2$ | $\frac{3}{4}a_3A_1A_2^2, \frac{3}{4}a_3A_1A_2^2$ |
| | | $3\omega_1, 3\omega_2$ | $\frac{1}{4}a_3A_1^3, \frac{1}{4}a_3A_2^3$ |

In the remaining part of the discussion, we consider only the frequencies within one octave of the signal frequencies. Therefore, the frequencies higher than $2\omega_1$ and $2\omega_2$ are ignored.

Figure 2.2(a) gives an example of a two tone signal at the input of a noisy, nonlinear device and Figure 2.2(b) shows the output signal of that device. Since the coefficient a_2 appears in the amplitude of the DC-component (see Table 2.1), the average of the output signal is larger than zero. Furthermore, the contribution of the coefficient a_3 to the amplitude of the fundamental results in the signal amplitude reduction. Moreover, the output signal is noisy. The spectra of the signals in Figure 2.2 are shown in

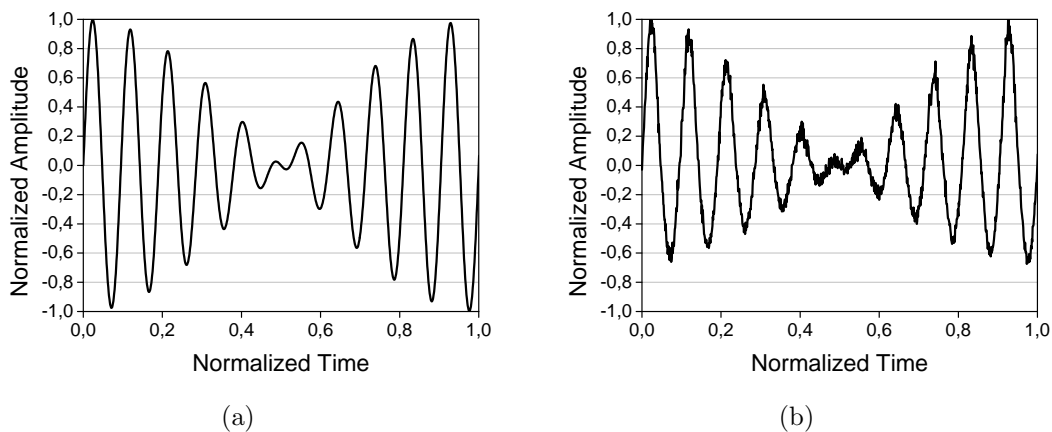


Figure 2.2: Input signal (a) and noisy, distorted output signal (b).

Figure 2.3 in which the frequency components are indicated. The same observations can be made as we did in Figure 2.2. The spectrum of the output signal has a large DC component. Furthermore, the spectrum plots show that the relative power of the two signal tones ω_1 and ω_2 at the output is lower than at the input. This corresponds to the observed signal amplitude reduction. Moreover, the spectrum of the output signal is noisy. Besides, from the output signal spectrum plot can be derived the difference in consequences of the nonlinearities for narrow- and broadband signals. For narrowband signals, only the third order distortion is important. In terms of Figure 2.2(b) the frequencies $2\omega_1 - \omega_2$ and $2\omega_2 - \omega_1$ are important. For broadband signals the second order distortion also comes into play. In terms of Figure 2.2(b) the frequencies $\omega_1 + \omega_2$ and $\omega_2 - \omega_1$ also play an important role.

A measure of distortion is the intercept point at which the fundamental power and the intermodulation power are equal [5]. In Figure 2.4 the output powers versus the input (signal) power is shown, both on log scales. The power at which the fundamental and one of the distortion curves intersect is called the intercept point. Equations (2.11a) and (2.11b) describe the conditions for the second- and third-order intercept points, respectively. In these equations, P_F denotes the fundamental power, P_{IM_2} denotes the second-order intermodulation power and P_{IM_3} denotes the third-order intermodulation power.

$$P_F = P_{IM_2} \quad (2.11a)$$

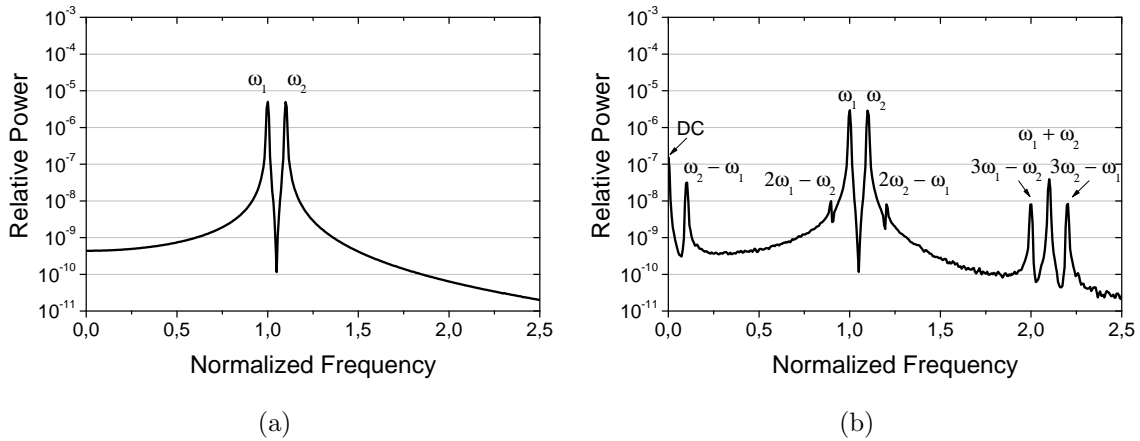


Figure 2.3: Spectrum of the input signal (a) and output signal (b) of Figure 2.2.

$$P_F = P_{IM_3} \quad (2.11b)$$

When doing distortion measurements, the fundamental, the second-order and the third-order powers at the output of the AOL are measured. Therefore, it is convenient to use the output as reference for the intercept points. As a result, the second-order and the third-order intercept points are referred to as the second-order and the third-order output intercept points (OIPs), respectively. Since every system has its own second- and third-order OIPs, these points are useful measures for the system performance. The higher the intercept points, the lower is the distortion for a given fundamental (or desired output signal) power. To avoid serious distortion, practical systems are always operated below these points.

2.5 Spurious Free Dynamic Range (SFDR)

In order to compare the performance of different AOLs, another measure is defined. This measure is the spurious free dynamic range (SFDR) which accounts for the noise power as well as the intermodulation power. Let the minimum power that a link can convey, p_{\min} , be the fundamental power corresponding to the intersection of the fundamental power and the noise power. Furthermore, let the maximum power, p_{\max} that a link can convey without any measurable distortion, be the fundamental power corresponding to the intersection of the distortion power and the noise power [5]. The ratio between this p_{\max} and p_{\min} is the SFDR. It is indicated in Figure 2.5 for the second-order and third-order intermodulation products, IM_2 and IM_3 , as $SFDR_2$ and $SFDR_3$, respectively. Because of symmetry, the SFDR can be drawn along the input power axis as well as along the output power axis. From this notion, the SFDR can also be defined as the SNR corresponding to the intersection of distortion and noise powers.

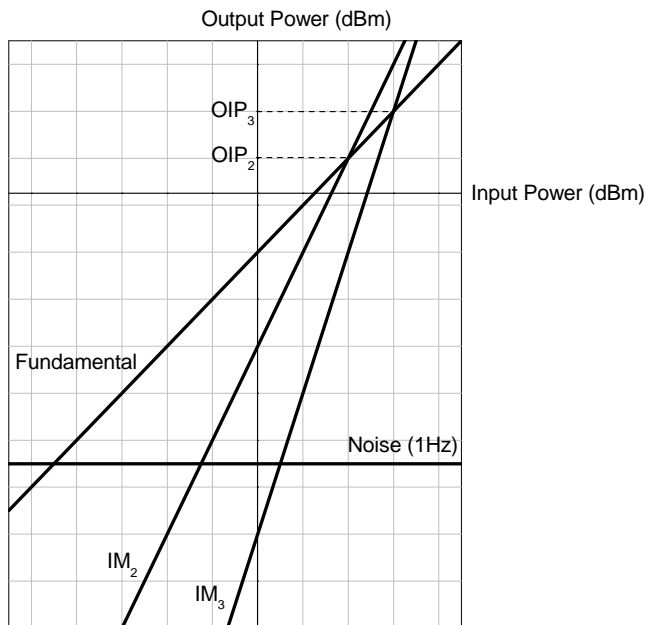


Figure 2.4: Plot of the fundamental output power, the second-order and third-order intermodulation output powers as a function of the input power for defining the second- and third-order OIPs.

It is convenient to express the SFDR in an 1-Hz noise bandwidth. By using the appropriate scaling law, the 1-Hz number can be scaled to any desired bandwidth. The general scaling law is given by [5] as:

$$SFDR_n [bw] = SFDR_n [1 \text{ Hz}] \cdot (bw)^{-\frac{n-1}{n}} \quad (2.12a)$$

or in dB:

$$SFDR_n [bw] = SFDR_n [1 \text{ Hz}] - \frac{(n-1)}{n} BW \quad (2.12b)$$

An illustration of the scaling laws is shown in Figure 2.6. In Figure 2.6(a) the increase in $SFDR_2$ for 40 dB decrease in noise power (1 Hz) is shown. In the initial case the $SFDR_2$ is 70 dB (Δ_1). After decreasing the noise level, the $SFDR_2$ becomes 90 dB (Δ_2). This corresponds to a change of 20 dB in $SFDR_2$ ($\Delta SFDR_2$). Therefore, $SFDR_2$ scales as $-\frac{1}{2}BW$ with BW the bandwidth in dB and as $(bw)^{-\frac{1}{2}}$ with bw the linear bandwidth. Note that a 40 dB increase in the noise bandwidth has the same result as increasing the noise power by 40 dB in the original noise bandwidth. A similar approach is followed for the $SFDR_3$ as shown in Figure 2.6(b). A 40 dB decrease in noise power corresponds to 26.7 dB increase in $SFDR_3$. As a result, $SFDR_3$ scales as $-\frac{2}{3}BW$ with BW the bandwidth in dB and as $(bw)^{-\frac{2}{3}}$ with bw the linear bandwidth.

Suppose the $SFDR_2$ (in dB) for unity bandwidth is known and it is desired to convert this to a bandwidth of 1.0 GHz. First, one has to calculate the ratio of these

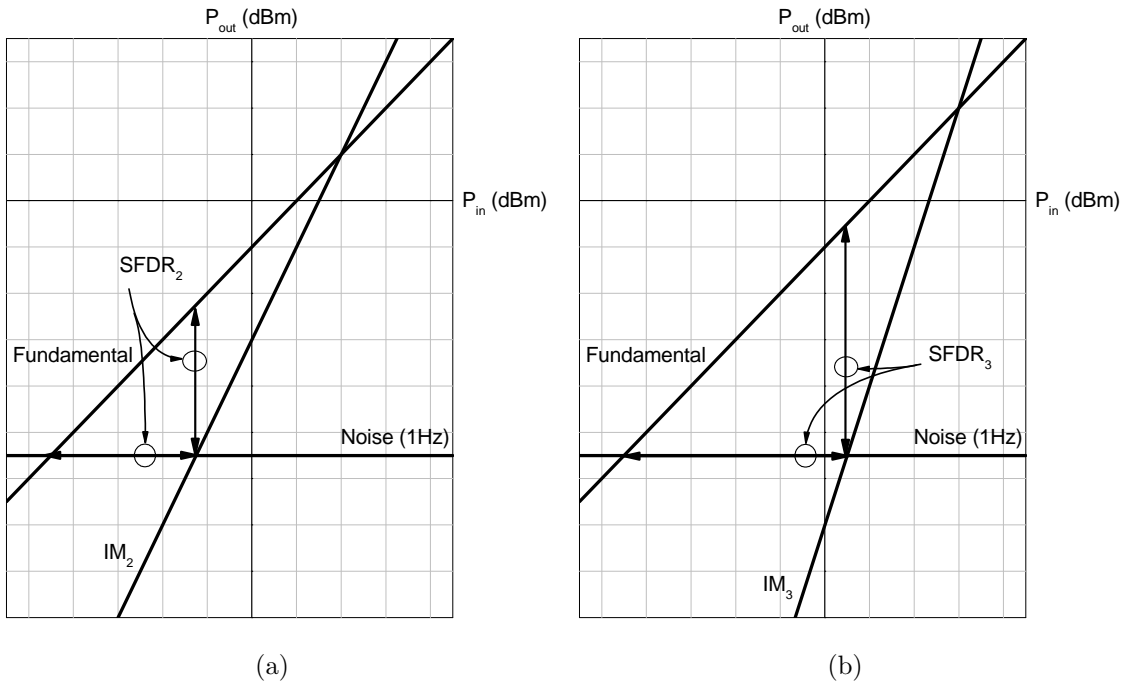


Figure 2.5: Plot of the fundamental output power, the second-order and third-order intermodulation output powers as a function of the input power for defining the SFDR₂ (a) and SFDR₃ (b).

two bandwidths, which is 90 dB. Secondly, one has to apply the scaling law, $-\frac{1}{2}BW$, resulting in $SFDR_2$ (1 GHz) = $SFDR_2$ (1 Hz) - 45 dB. Taking another example for $SFDR_3$ of scaling from unity bandwidth to 1.0 GHz bandwidth, one obtains $SFDR_3$ (1 GHz) = $SFDR_3$ (1 Hz) - 60 dB.

The above discussed scaling law in Equation (2.12) appears also in the relation between SFDR and OIP. This relation is mathematically expressed in Equation (2.13). In Appendix A, the relation between SFDR and OIP is discussed in more detail.

$$SFDR_n \text{ [dB]} = \frac{(n-1)}{n} \left(OIP_n \text{ [dBm]} - N_{out} \text{ [dBm]} \right) \quad (2.13)$$

2.6 Numerical Example

The concept of SFDR is illustrated by a numerical example. We consider an IMDD-link of which the link parameters are listed in Table 2.2. In this example, four different situations are calculated by changing three link parameters. The situations and corresponding calculated results are listed in Table 2.3. In the first situation, all the link parameters are set to their initial values. In the other situations, only one parameter differs from its initial value. The change in parameter settings affects the noise level, resulting in other SFDR values. In other words, this example illustrates three parameters affecting the SFDR.

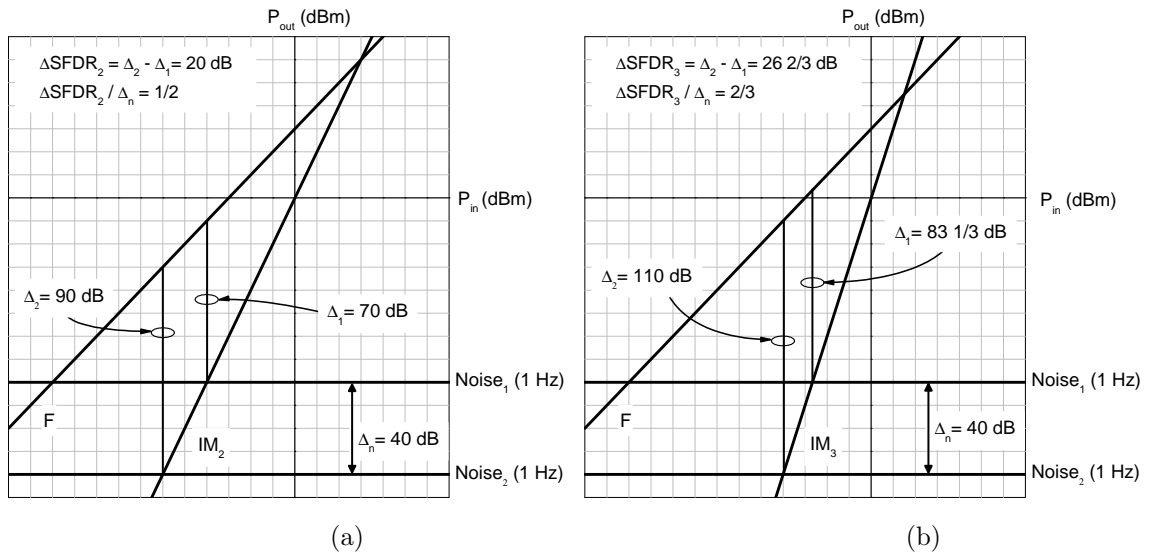


Figure 2.6: Plot of $SFDR_2$ (a) and $SFDR_3$ (b) for two different noise power levels.

Table 2.2: The simulation parameters for numerical example

| Parameter | Symbol | Value | Units |
|---|---------------|-------|----------|
| laser slope efficiency | s_1 | 0.3 | W/A |
| photodetector responsivity | R_{pd} | 0.8 | A/W |
| laser RIN power spectral density | RIN_{laser} | -155 | dB/Hz |
| load resistance | R_{load} | 50 | Ω |
| input resistance | R_{in} | 50 | Ω |
| absolute temperature | T | 293 | K |
| noise bandwidth | bw | 10 | MHz |
| laser threshold current | I_t | 15 | mA |
| laser bias current | I_1 | 75 | mA |
| power level second-order output intercept point | OIP_2 | 43.6 | dBm |
| power level third-order output intercept point | OIP_3 | 20.6 | dBm |
| link gain | G_{link} | -12.4 | dB |

Table 2.3: The four simulated situations in the numerical example

| Situation | Changed Parameter | New Value | Noise level (dBm) | $SFDR_2$ (dB) | $SFDR_3$ (dB) |
|-----------|-------------------|------------|-------------------|---------------|---------------|
| 1 | - | - | -49.98 | 46.8 | 47.1 |
| 2 | RIN_{laser} | -120 dB/Hz | -15.05 | 29.3 | 23.8 |
| 3 | I_1 | 100 mA | -46.97 | 45.3 | 45.0 |
| 4 | bw | 100 MHz | -39.98 | 41.8 | 40.4 |

Ideal Class-B AOL

In this chapter the characteristics of the ideal Class-B optical link are discussed. This discussion evaluates the ideal Class-B optical link performance using the conventional IMDD link as a benchmark.

3.1 Principle of Class-B in AOL

As discussed in the previous chapter, there is a demanding need for links in which all received optical power contributes to the RF-signal power. Moreover, a quadratic relation between optical power and RF-signal power is required. In other words, there is a demanding need for Class-B operation in AOLs or links having the ideal response of Figure 1.1.

In an ideal Class-B optical link, the dc-bias link operation is avoided by linearly converting the modulating RF-signal into a pair of complementary half-wave rectified optical signals [3]. An illustration is shown in Figure 3.1(a) for a sinusoidal input signal. Due to this half-wave rectification (HWR), optical power is transmitted only in the presence of an RF-signal. As a result, the optical power becomes a function of the RF-signal, as is shown for both signal parts. In Figure 3.2 the ideal response of the HWR is shown. In order to restore the original RF-signal, both complementary half-wave rectified optical signals need to be detected. Furthermore, the detected complementary signals have to be subtracted from each other. These two processes can be carried out by a differential detection scheme. In other words, a modulation device employing HWR and a differential detector are needed to implement a Class-B optical link, as is shown in Figure 3.1(b).

3.2 Noise

As is discussed in section 2.3, shot noise and RIN depend linearly and quadratically on optical power, respectively. Therefore, they depend on the RF-signal in a Class-B

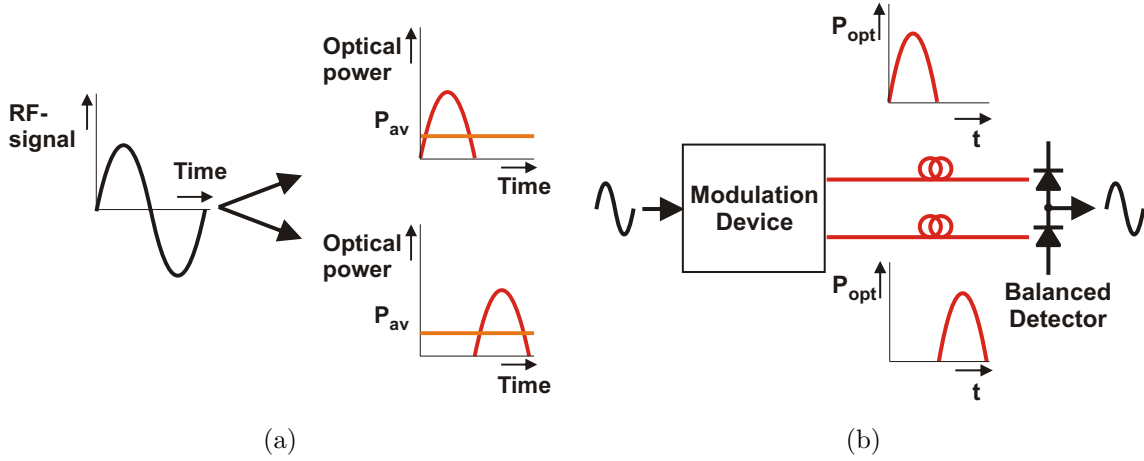


Figure 3.1: Dc-bias suppression by HWR (a) and the ideal Class-B optical link (b)

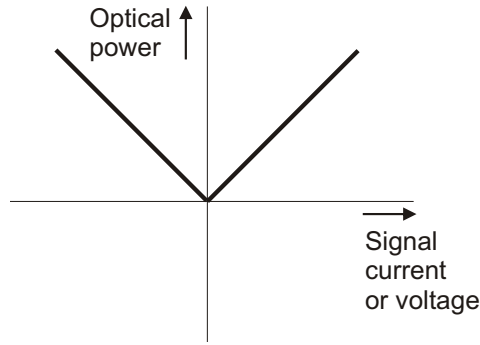


Figure 3.2: Ideal response for HWR

optical link [2], [3]. To illustrate the advantage of this, the theoretical approach in [2] is followed. In this work the Class-B optical link is constructed using a balanced pair of directly modulated lasers as modulation device.

In order to evaluate the Class-B noise performance, a mathematical description for the average optical power per branch is needed. We assume that both branches have equal average optical power, such that we only need to determine the optical power of one branch. Considering the upper branch of the scheme in Figure 3.1(b), its optical power, P_{op} , is mathematically expressed as:

$$P_{op} [\text{W}] = \begin{cases} s_1 i_1 \sin \frac{2\pi t}{T} & \text{for } 0 < t \leq \frac{T}{2} \\ 0 & \text{for } \frac{T}{2} < t \leq T \end{cases} \quad (3.1)$$

In Equation (3.1), s_1 denotes the laser slope efficiency (in W/A), i_1 denotes the laser RF-current amplitude (in A), t denotes the time and T denotes the period time. The

average of this power, $\langle P_{\text{op,CB}} \rangle$, is as follows:

$$\begin{aligned} \langle P_{\text{op,CB}} \rangle [\text{W}] &= \frac{1}{2\pi} \left(\int_0^{\frac{T}{2}} s_1 i_1 \sin \frac{2\pi t}{T} dt + \int_{\frac{T}{2}}^T 0 dt \right) \\ &= \frac{s_1 i_1}{\pi} \end{aligned} \quad (3.2)$$

By using the Equations (2.3), (2.5) and (3.2), the RIN and shot noise powers in the upper branch can be determined. By considering the noise processes of the upper branch to be independent of the lower branch, the total shot noise and RIN power is two times that of the upper branch.

Furthermore, to simulate the performance of a conventional IMDD link for using it as a benchmark, a description of its average optical power $\langle P_{\text{op,IMDD}} \rangle$ is needed. The average optical power is dependent on the biasing of the laser, or the laser bias current I_1 (in A), and the laser threshold current I_t , and is written as:

$$\langle P_{\text{op,IMDD}} \rangle [\text{W}] = s_1 \cdot (I_1 - I_t) \quad (3.3)$$

By using the Equations (2.3), (2.5) and (3.3), the RIN and shot noise powers in the conventional IMDD link can be determined.

The noise powers (in 10 MHz effective noise bandwidth) of both links are simulated in LabVIEW 8.5. The parameters used in the simulations are listed in Table 3.1. Using these parameters and Equations (3.2) and (3.3), results in the same link gain for both links, $G_{\text{link,CB}} = G_{\text{link,IMDD}} = -12.40$ dB.

Table 3.1: Simulation parameters for noise performance analysis of Class-B and IMDD optical links

| Parameter | Symbol | Value | Units |
|----------------------------------|----------------------|-------|----------|
| laser slope efficiency | s_1 | 0.3 | W/A |
| photodetector responsivity | R_{pd} | 0.8 | A/W |
| laser RIN power spectral density | RIN_{laser} | -155 | dB/Hz |
| load resistance | R_{load} | 50 | Ω |
| input resistance | R_{in} | 50 | Ω |
| absolute temperature | T | 293 | K |
| noise bandwidth | bw | 10 | MHz |
| laser threshold current* | I_t | 15 | mA |
| laser bias current** | I_1 | 75 | mA |

* = also bias point for lasers in Class-B optical link simulation

** = only for IMDD optical link simulation: most linear operating point

The simulation results are shown in Figure 3.3. It shows the RF-input power independence of the noise in the IMDD optical link. The most dominant noise source

is RIN. Furthermore, the figure shows the RF-input power dependence of the RIN and the shot noise in the Class-B optical link. For low RF-input power, the total link noise is equal to the thermal noise power. When the RF-input power becomes larger, the shot noise comes into play and ultimately the RIN becomes dominant.

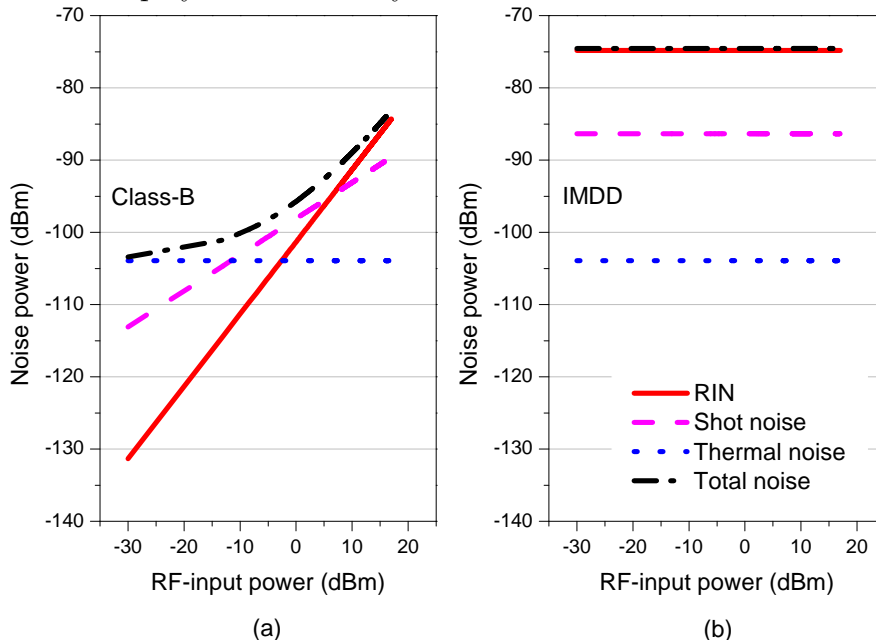


Figure 3.3: Simulation results of an ideal Class-B (a) and an IMDD (b) optical link: Noise power ($bw = 10$ MHz) versus RF-input power.

To get a better impression of these results, the SNR of both links is shown in Figure 3.4. It is evident from this figure that the Class-B optical link gives a significant advantage over the conventional IMDD optical link in a wide range of RF-input powers. Notably in the small signal region, where the SNR is premium, an impressive SNR improvement of 29 dB has been achieved.

3.3 Distortion

The distortion analysis of the Class-B optical link is beyond the scope of this report. For an analysis based on the BMD scheme, where a balanced pair of directly modulated lasers are used as modulation device, the reader is referred to the work of [2].

3.4 Dynamic Range

Since the RIN and the shot noise in the Class-B optical link are a function of the RF-signal, the SFDR can not be used as performance measure. Therefore, we use another performance measure for Class-B optical links. It is the range of RF-power which

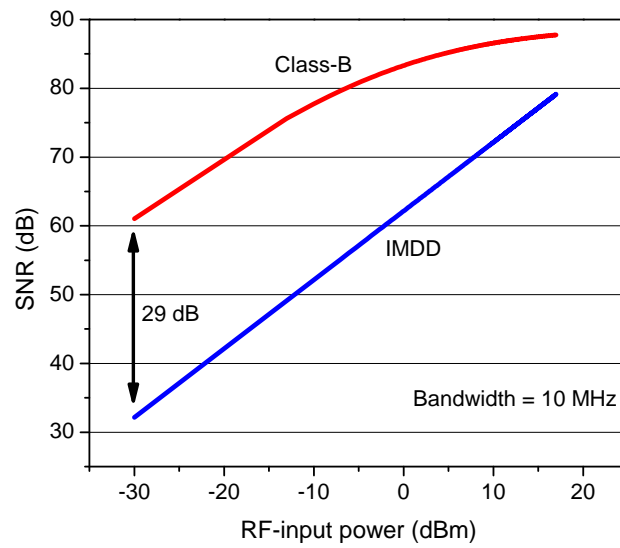


Figure 3.4: Simulation results of an ideal Class-B and an IMDD optical link: SNR versus RF-input power.

satisfies both a minimum required SNR and a minimum required signal-to-distortion ratio (SDR). The SDR is the ratio between the fundamental power and the distortion power. A theoretical analysis of this measure is beyond the scope of this report [2], [4].

Frequency Modulation-Slope Detection Analog Optical Link

In this chapter the frequency modulation (FM)-slope detection AOL realizing the Class-B optical link is discussed. The FM combined with the slope detection in the FM-slope detection AOL are employed to obtain half-wave rectification (HWR). Later on, this chapter is used as starting point in the filter design, where the designed optical filter has to perform the slope detection.

4.1 Frequency Modulation-Slope Detection Scheme

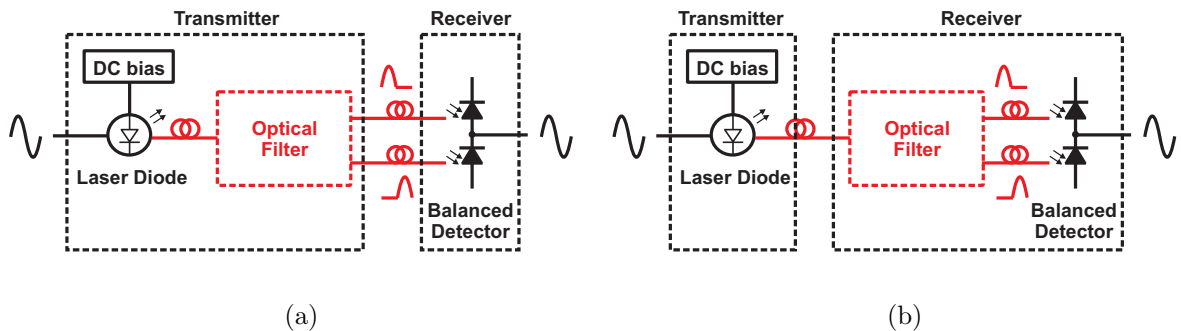


Figure 4.1: FM-slope detection AOL.

The proposed link consists of a directly modulated laser, an optical filter acting as slope detector and a balanced detector, as is shown in Figure 4.1(a). To be consistent with Figure 3.1(b), the SLD combined with the optical filter is indicated as 'Transmitter', but the optical filter can also be part of the 'Receiver', as is shown in Figure 4.1(b). This last implementation is more practical, since a single fiber is needed for connecting the transmitter and receiver ends.

In both schemes of Figure 4.1 the frequency chirping characteristic of an SLD is employed generating a frequency modulated optical carrier. The instantaneous frequency

deviation linearly corresponds to the instantaneous amplitude of the RF-signal, as is shown in Figure 4.2 (a) [7]. In this figure the ideal frequency response of the laser chirp as function of the modulating RF-current is shown. The maximum RF-current is denoted by Δ_m and the maximum optical frequency deviation is denoted by Δ_f .

As a result of direct modulation of the SLD, not only the frequency but also the intensity of the carrier is modulated. Therefore, a frequency as well as an intensity modulated optical carrier will be present at the filter input. To simplify the discussion intensity modulation is neglected at this point.

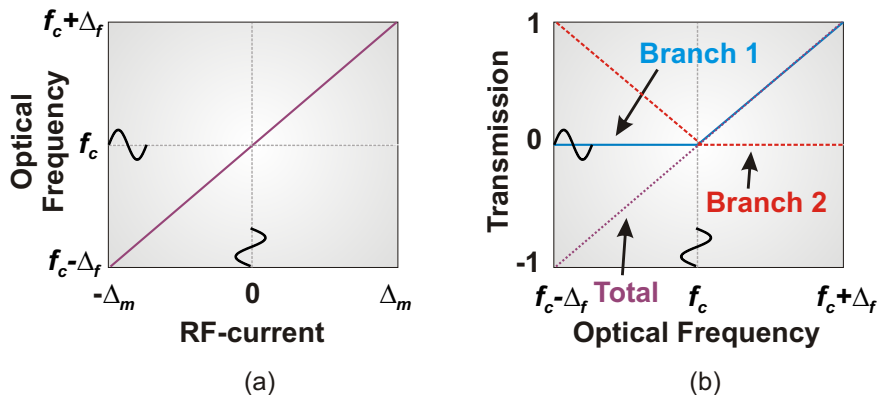


Figure 4.2: Ideal chirp transfer (a) and ideal slope transfer (b)

The optical filter has two branch outputs of which ‘Branch 1’ linearly converts the optical frequencies higher than f_c into intensity and ‘Branch 2’ does the same for frequencies lower than f_c , as is shown in Figure 4.2 (b). In this way, FM to IM conversion will yield two optical signals that comprise complementary half-wave rectified versions of the original modulating RF-signal. Since the transmission is zero at the carrier frequency, f_c , for both branches, the optical power of the laser is suppressed. The balanced detector then detects the optical signals, resulting in the total filter response of Figure 4.2 (b).

Above, it was pointed out that the carrier at the filter input is modulated in its frequency as well as in its intensity. In the RF-domain a similar situation occurs when employing FM. Variations in the carrier amplitude are induced by the FM transmitter or by variations in the signal path from transmitter to receiver. In order to reduce the signal level changes a signal limiter is used in the FM receiver. To our knowledge however, there are no intensity limiters in the optical domain to cancel the intensity modulation of the laser. For now, we only assume that the frequency modulation index is much larger than the intensity modulation index of the laser. Later on, measurements must validate the assumption of negligible intensity modulation.

Filter Design and Simulation

This chapter discusses the design of the slope detector of which the general requirements are described in Chapter 4. The discussion starts with the design requirements. Next, the choice of building blocks is discussed. Then, several designs are made and simulated in LabVIEW 8.5. In this last design stage, a simple concept is improved step-by-step. The discussion ultimately arrives at the final design.

5.1 Design Requirements

The main design constraint is to realize the ideal filter response in Figure 4.2 (b) without having an extremely complicated structure. A complicated structure is not only difficult to fabricate, but it also complicates the simulation. To ensure proper HWR, the branch transfers must have an instantaneous transition from the flat to the linear response around the carrier frequency. In Figure 5.1 three examples are shown of improper transitions at the carrier frequency. Misalignment of the branch transfers (case 1) leads to distortion. Besides, power leakage at the carrier frequency can occur when the passbands of the branch transfers have an overlap (case 2). Moreover, gradual transitions (case 3) will result in distortion and power leakage at the carrier frequency.

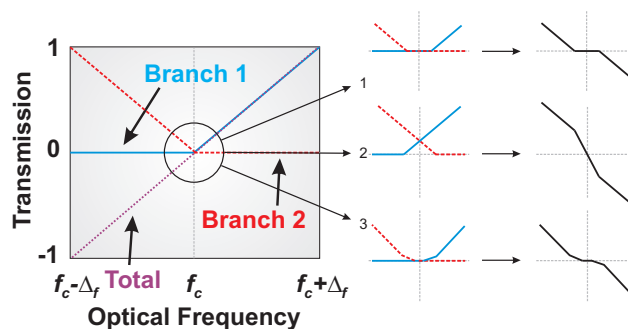


Figure 5.1: Filter transfer

Another important constraint is to make the slope detector integratable with the

balanced detector, resulting in a small receiver device. Therefore, it is required to have a design based on an integrated chip. Furthermore, it is desirable to have a tunable slope detector to compensate fabrication tolerances and for flexibility purposes. In this way, it is taken into advance the possibility of using the same filter for different optical FM-sources. It is assumed that the FM-index is large enough to neglect the IM-index, so there is not accounted for the laser IM response in the design.

5.2 Digital Filter Design Approach

In [8] it is pointed out that the digital signal processing techniques are relevant to optical filters, because they are linear, time-invariant systems that have discrete delays. Just as is the case for digital filters, optical filters have splitters, delays and combiners as basic elements. Therefore, the filter design is based on digital signal processing concepts.

Digital filters are described by the Z-transform. The Z-transform is an analytical extension of the discrete-time Fourier transform for discrete signals. Consider the discrete-time Fourier transform of a discrete signal, $x(k)$:

$$X(\omega) = \sum_{k=-\infty}^{\infty} x(k)e^{-j\omega k} \quad (5.1)$$

Its Z-transform is obtained by substituting z for $e^{j\omega}$ as follows:

$$X(z) = \sum_{k=-\infty}^{\infty} x(k)z^{-k} \quad (5.2)$$

In the Z-transform description z^{-1} represents the unit delay. It is noted that a filter having impulse response $h(k)$ must satisfy the condition $h(k) = 0$ for $k < 0$ in order to be causal.

The unit delay, T_U , in optical filters is defined as follows:

$$T_U = \frac{L_U n}{c} \quad (5.3)$$

In Equation (5.3) denotes n the group index, c the speed of light and L_U the unit delay or smallest path length difference. In general, the optical path lengths in an optical filter are integer multiples of the unit delay length, resulting in a periodic frequency response. One period of the frequency response is defined as free spectral range (FSR) and is mathematically expressed as follows:

$$f_{\text{FSR}} = \frac{1}{T_U} = \frac{c}{L_U n} \quad (5.4)$$

5.3 Available Components for Design

The slope detector must be fabricated in an optical chip, resulting in a limited number of filter stages or number of delay elements. As a result, the ideal response can only be approximated. Furthermore, the filter components which can be realized in an optical chip are directional coupler (DC), ring-resonator and Mach-Zehnder interferometer (MZI). The schematics of these components are shown in Figure 5.2. Note that the DC is part of the MZI and the ring-resonator.

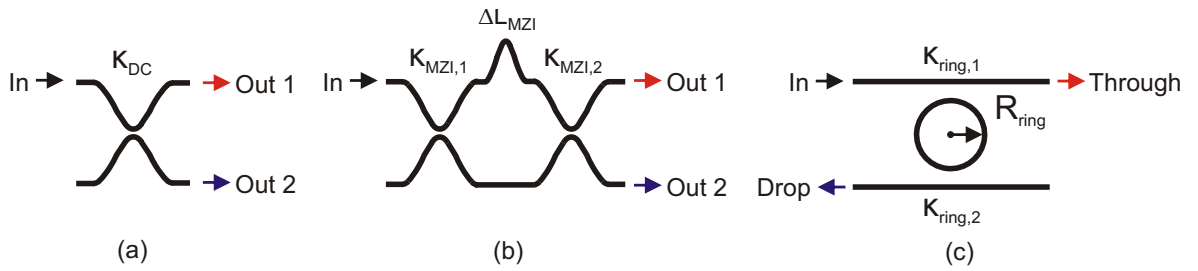


Figure 5.2: Available filter components: (a) DC, (b) MZI and (c) ring-resonator.

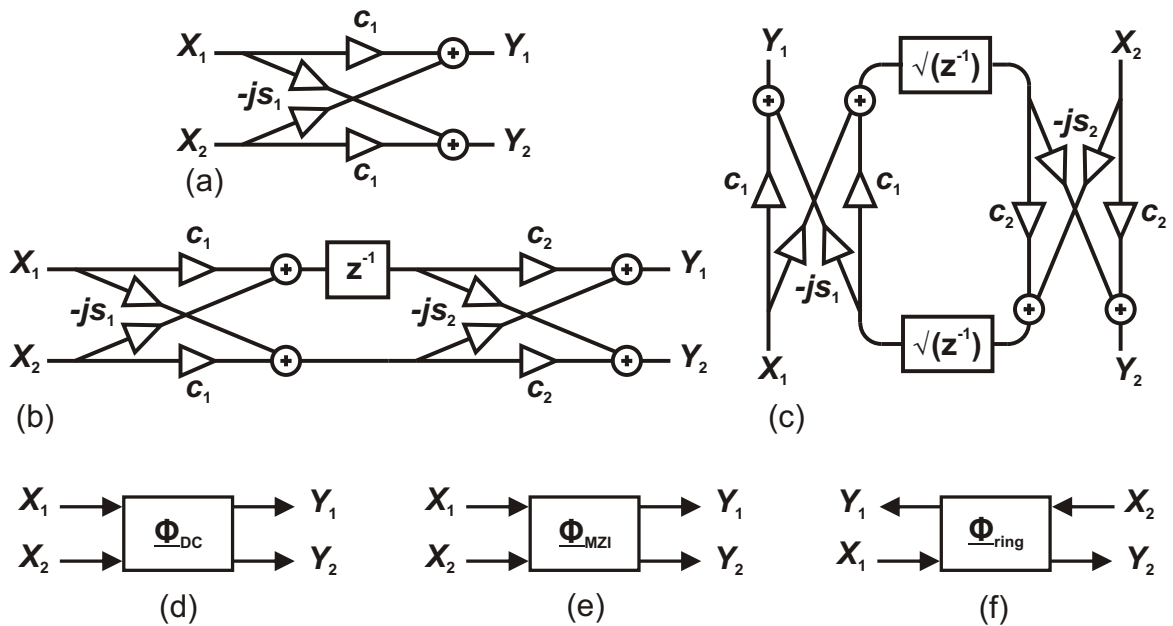


Figure 5.3: Z-transform schematics of (a) DC, (b) MZI and (c) ring-resonator, and transfer matrix representations of (d) DC, (e) MZI and (f) ring-resonator.

It is useful to consider the transfer functions of the components. For this, the Z-transform schematics are considered first, which are shown in Figure 5.3. In this figure X_1 and X_2 represent the input field amplitudes and Y_1 and Y_2 represent the output field amplitudes. Furthermore, the through- and cross-port transmissions are respectively designated by c and $-js$. Those are related to the power coupling coefficient κ as

follows:

$$c = \sqrt{1 - \kappa} \quad (5.5a)$$

$$-js = -j\sqrt{\kappa} \quad (5.5b)$$

Note that the sum of the squares of the transmission is 1 or:

$$c^2 + (-js)^2 = (\sqrt{1 - \kappa})^2 + (-j\sqrt{\kappa})^2 = 1 \quad (5.6)$$

In other words, the sum of the transmission powers is equal to 1, thereby fulfilling the power conservation condition.

5.3.1 Directional Coupler

The Z-transform of the directional coupler (DC) is shown in Figure 5.3 (a). Using this Z-transform the 2×2 transfer matrix, Φ_{DC} , can be derived. This matrix describes the relations between the input and output fields for the DC as in Equation 5.7. The matrix is shown in Figure 5.3 (d).

$$\begin{aligned} \begin{bmatrix} Y_1 \\ Y_2 \end{bmatrix} &= \begin{bmatrix} c & -js \\ -js & c \end{bmatrix} \begin{bmatrix} X_1 \\ X_2 \end{bmatrix} \\ &= \Phi_{\text{DC}}(\kappa) \begin{bmatrix} X_1 \\ X_2 \end{bmatrix} \end{aligned} \quad (5.7)$$

Consider the case where an optical power is present at the 'In'-port, as indicated in Figure 5.2 (a). A large directional coupler power coupling coefficient, κ_{DC} , results in more power coupling to the 'Out 2'-port, since the power coupling is proportional to κ_{DC} . Furthermore, it results in less power coupling to the 'Out 1'-port, since here the power coupling is proportional to $1 - \kappa_{\text{DC}}$. The response of the DC for $\kappa_{\text{DC}} = 0.75$ is shown in Figure 5.4. In this figure 'Out 1' and 'Out 2 correspond to Figure 5.2 (a). Furthermore, Y_1 and Y_2 correspond to Figure 5.3 (a) and (d). Note that the 'In' or X_1 -port, depending on the considered figure, is the input.

5.3.2 Mach-Zehnder Interferometer

The Z-transform of the Mach-Zehnder interferometer (MZI) is shown in Figure 5.3 (b). It is a cascade of two DCs and a section representing the branches between the two DCs. In this section the unit delay represents the difference in path length, ΔL_{MZI} , between the branches. In other words, the longer branch has a transfer function of z^{-1} relative to the shorter branch. This can be described by a 2×2 transfer matrix as follows:

$$\Phi_{\text{delay}} = \gamma e^{-j\beta L_{\text{MZI}}} \begin{bmatrix} z^{-1} & 0 \\ 0 & 1 \end{bmatrix} \quad (5.8)$$

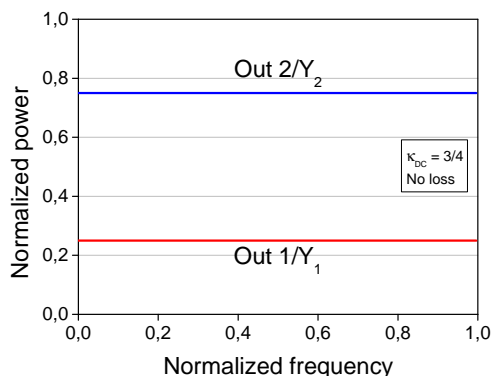


Figure 5.4: DC response

In Equation (5.8) γ represents the field loss in the common path length, L_{MZI} , of both branches. This loss is expressed in Equation (5.9), where α is the average power loss in dB per unit length and L is the propagation length. Since the difference in length, ΔL_{MZI} , is much smaller than the common path length, L_{MZI} , of the branches, the loss in ΔL_{MZI} is neglected. Furthermore, in Equation (5.8) $e^{-j\beta L_{\text{MZI}}}$ represents the linear phase contribution of the common path-lengths L_{MZI} , where β is the propagation constant.

$$\gamma = 10^{\frac{-\alpha L}{20}} \quad (5.9)$$

Using the transfer matrices of the DC and the delay section, the 2×2 transfer matrix of the MZI, Φ_{MZI} , can be derived as in Equation (5.10). Figure 5.3 (e) shows the transfer matrix of the MZI.

$$\begin{aligned} \Phi_{\text{MZI}} &= \Phi_{\text{DC}}(\kappa_2) \Phi_{\text{delay}} \Phi_{\text{DC}}(\kappa_1) \\ &= \gamma e^{-j\beta L_{\text{MZI}}} \begin{bmatrix} c_2 & -js_2 \\ -js_2 & c_2 \end{bmatrix} \begin{bmatrix} z^{-1} & 0 \\ 0 & 1 \end{bmatrix} \begin{bmatrix} c_1 & -js_1 \\ -js_1 & c_1 \end{bmatrix} \\ &= \gamma e^{-j\beta L_{\text{MZI}}} \begin{bmatrix} -s_1 s_2 + c_1 c_2 z^{-1} & -j(c_1 s_2 + s_1 c_2 z^{-1}) \\ -j(s_1 c_2 + c_1 s_2 z^{-1}) & c_1 c_2 - s_1 s_2 z^{-1} \end{bmatrix} \end{aligned} \quad (5.10)$$

From now on we disregard the linear phase contribution of the common path lengths to simplify the discussion.

Consider the lossless case ($\gamma = 1$) where $\kappa_{\text{MZI},1} = \kappa_{\text{MZI},2} = 0.5$. Substitution of $z^{-1} = e^{-j\omega$ will give the complete frequency response after some calculations and rearrangements as:

$$\begin{aligned} |H_{11}(\omega)|^2 &= |H_{22}(\omega)|^2 = \sin^2 \left(\frac{\omega T}{2} \right) \\ |H_{12}(\omega)|^2 &= |H_{21}(\omega)|^2 = \cos^2 \left(\frac{\omega T}{2} \right) \end{aligned} \quad (5.11)$$

In Equation (5.11) $H_{ij}(\omega)$ denotes the frequency response from port X_j to port Y_i . The frequency response is simulated in LabVIEW 8.5. In the simulation program, the

frequency is normalized and the relative length difference of the MZI branches, ΔL_{MZI} , is expressed as a phase shift. Therefore, the normalized FSR and the phase can be set. For the MZI response plot, the FSR is set to 1, the phase is set to 0 and the power coupling coefficients are set to 0.5. The simulation results are shown in Figure 5.5. In this figure ‘Out 1’ and ‘Out 2’ correspond to Figure 5.2 (b). Furthermore, Y_1 and Y_2 correspond to Figure 5.3 (b) and (e). Note that the ‘In’ or X_1 -port, depending on the considered figure, is the input.

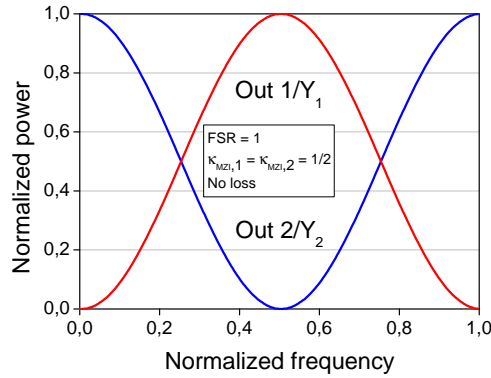


Figure 5.5: MZI response

5.3.3 Ring Resonator

The Z-transform of the ring-resonator is shown in Figure 5.3 (c). In this Z-transform z^{-1} represents the perimeter of the ring. The Z-transform of the ring is more complex than that of the DC and MZI. Therefore, we briefly discuss the responses before deriving the ring resonator transfer matrix, Φ_{ring} . Considering Y_2 as output and X_1 as input, then Y_2 can be described as follows:

$$Y_2(z) = -s_1 s_2 \sqrt{\gamma z^{-1}} \{1 + c_1 c_2 \gamma z^{-1} + (c_1 c_2 \gamma z^{-1})^2 + \dots\} X_1(z) \quad (5.12)$$

In Equation (5.12) the terms before X_1 is the sum of all optical paths. The term outside brackets, $-s_1 s_2 \sqrt{\gamma z^{-1}}$, is the transmission from the input to the output without the feedback path connected. The second term inside the brackets, $c_1 c_2 \gamma z^{-1}$, is the propagation once around the ring. The third term, inside brackets $(c_1 c_2 \gamma z^{-1})^2$, is the propagation twice around the ring and so on. This infinite sum can be rewritten in the finite form of Equation (5.13).

$$\begin{aligned} H_{21}(z) &= \frac{Y_2(z)}{X_1(z)} = \frac{-\sqrt{\kappa_{\text{ring},1} \kappa_{\text{ring},2} \gamma z^{-1}}}{1 - c_1 c_2 \gamma z^{-1}} \\ &= \frac{-\sqrt{\kappa_{\text{ring},1} \kappa_{\text{ring},2} \gamma z^{-1}}}{A(z)} \end{aligned} \quad (5.13)$$

Consider now Y_1 as output and X_1 as input. Then Y_1 can be described as in Equation (5.14). In this equation the terms before X_1 is the sum of all optical paths. The c_1 term is the transmission from the input to the output without the feedback path connected. The $-s_1^2 c_2 \gamma z^{-1}$ term is the transmission from the input to the output once around the ring and so on. The corresponding transfer function is given by Equation (5.15).

$$\begin{aligned} Y_1(z) &= [c_1 - s_1^2 c_2 \gamma z^{-1} \{1 + c_1 c_2 \gamma z^{-1} + (c_1 c_2 \gamma z^{-1})^2 + \dots\}] X_1(z) \\ &= \left[\frac{c_1 - c_2 \gamma z^{-1}}{1 - c_1 c_2 \gamma z^{-1}} \right] X_1(z) \end{aligned} \quad (5.14)$$

$$\begin{aligned} H_{11}(z) &= \frac{Y_1(z)}{X_1(z)} = \left[\frac{c_1 - c_2 \gamma z^{-1}}{1 - c_1 c_2 \gamma z^{-1}} \right] \\ &= \frac{B(z)}{A(z)} \end{aligned} \quad (5.15)$$

Similarly, one can obtain H_{12} and H_{22} and derive the relations in Equations (5.16) and (5.17). In Equation (5.17) $B^R(z)$ is the reverse polynomial of $B(z)$; the superscript R denotes reverse polynomial.

$$H_{12}(z) = H_{21}(z) = \frac{-\sqrt{\kappa_{\text{ring},1} \kappa_{\text{ring},2} \gamma z^{-1}}}{A(z)} \quad (5.16)$$

$$\begin{aligned} H_{22}(z) &= \frac{Y_2(z)}{X_2(z)} = \left[\frac{c_2 - c_1 \gamma z^{-1}}{1 - c_1 c_2 \gamma z^{-1}} \right] \\ &= \frac{-B^R(z)}{A(z)} \end{aligned} \quad (5.17)$$

Now the transfer functions are derived, the frequency responses of the ring can be considered. Consider the case where the coupling coefficients are equal, $\kappa_{\text{ring},1} = \kappa_{\text{ring},2} = \kappa$, then the square magnitude response of $H_{21}(\omega)$ is given by Equation (5.18). A transmission peak occurs at $\omega = \phi$, where ϕ is the phase of the ring. When the ring is lossless, the peak transmission is 1 ($\gamma = 1$).

$$|H_{21}(\omega)|^2 = \frac{\kappa^2 \gamma}{1 - 2c^2 \gamma \cos(\omega - \phi) + c^4 \gamma^2} \quad (5.18)$$

Now having the response of $H_{21}(\omega)$, it is easy to derive the response $H_{11}(\omega)$, since they are complementary. Furthermore, since $\kappa_{\text{ring},1} = \kappa_{\text{ring},2} = \kappa$, $-B^R(z) = B(z)$ resulting in $H_{22}(z) = H_{11}(z)$.

The frequency responses are simulated in LabVIEW 8.5. In the simulation program, the frequency and the radius of the ring, R_{ring} , are normalized. Therefore, the FSR

and the phase can be set. Since a large FSR is related to a small delay, a large FSR corresponds to a small ring radius R_{ring} . For the response plot, the FSR is set to 1, the phase is set to 0 and the power coupling coefficients are set to $\kappa_{\text{ring},1} = \kappa_{\text{ring},2} = 0.33$. Besides, the loss is set to zero ($\gamma = 1$).

Figure 5.6 shows the response plot of H_{11} and H_{21} . In the figure ‘Through’ (H_{11})

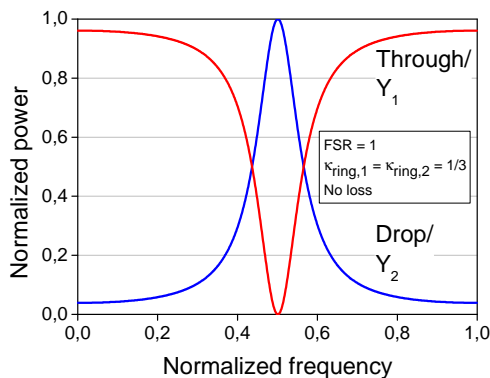


Figure 5.6: Response of ring with two couplers

and ‘Drop’ (H_{21}) correspond to Figure 5.2 (c). Furthermore, Y_1 and Y_2 correspond to Figure 5.3 (c) and (f). Note that the ‘In’ or X_1 -port, depending on the considered figure, is the input.

Since the H_{11} -response is high for a large frequency range and the H_{21} -response for a small frequency range, they are respectively denoted as ‘Through’-and ‘Drop’-responses. The H_{12} -response is called ‘Add’-response, since another signal with the same carrier frequency as that of the ‘Drop’-signal can be added via port X_2 . The width of the peak or valley is related to the power coupling coefficients. The smaller the coupling coefficients, the narrower the peak or valley. The loss in the ring will impact the peak height or valley depth.

Just as in the case of the MZI and the DC, the 2×2 transfer matrix of the ring-resonator, Φ_{ring} , is presented. The 2×2 transfer matrix of the ring resonator is shown in Figure 5.3 (f). After doing some mathematical operations, the transfer matrix is derived from Equations (5.15), (5.16) and (5.17) as:

$$\begin{bmatrix} Y_1(z) \\ X_1(z) \end{bmatrix} = \Phi_{\text{ring}}(z) \begin{bmatrix} X_2(z) \\ Y_2(z) \end{bmatrix} \quad (5.19)$$

$$\text{where } \Phi_{\text{ring}}(z) = \frac{1}{-\sqrt{\kappa_{\text{ring},1}\kappa_{\text{ring},2}\gamma z^{-1}}} \begin{bmatrix} A^R(z) & B(z) \\ B^R(z) & A(z) \end{bmatrix}$$

5.4 Slope Detector Design

At least two components for the slope detector design are needed to obtain the required branch responses of Figure 4.2 (b). Considering their output responses, it is impossible to obtain the required response using only one of the components of Section 5.3. Therefore, two relative simple filter designs, in which a directional coupler equally divides the input power, are used as starting point for the actual design.

5.4.1 DC Power Divider and Two MZIs

In the first design each DC-output is connected to an MZI as shown in Figure 5.7. By

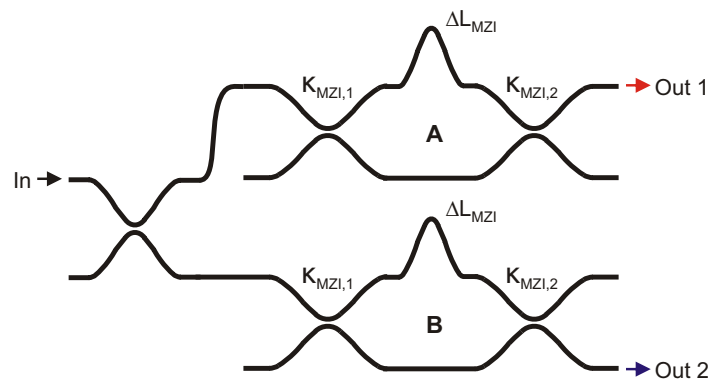


Figure 5.7: Design based on a DC power divider and two MZIs

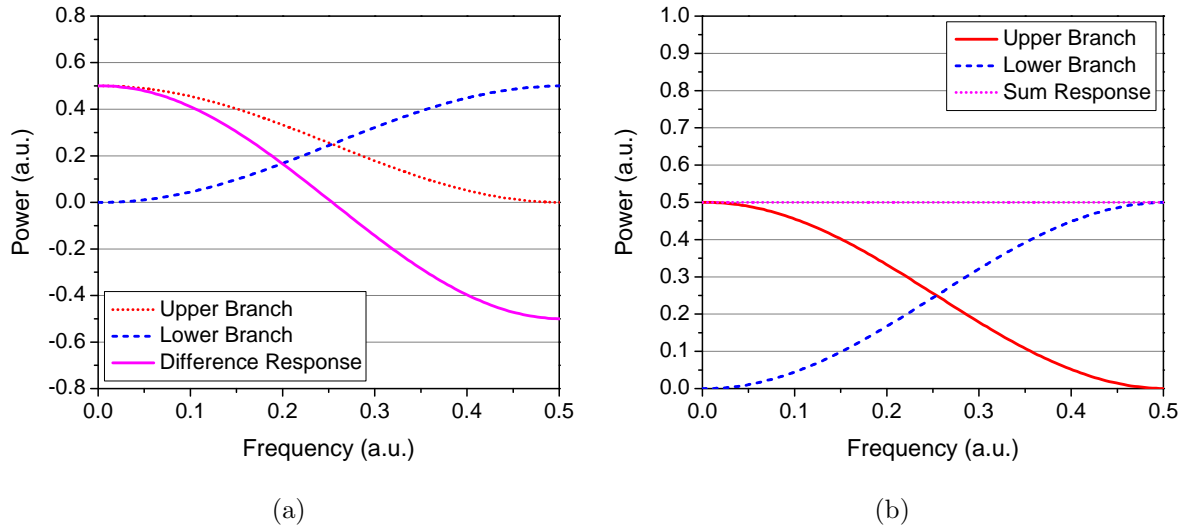
properly tuning and taking the linearity and total response high into consideration, the simulation parameters as listed in Table 5.1 are obtained. The resulting responses are shown in Figure 5.8. In this figure the ‘Upper Branch’ corresponds to ‘Out 1’ and ‘Lower Branch’ response corresponds to ‘Out 2’.

Consider the ‘Upper Branch’ response in Figure 5.8. It is the multiplication of the ‘Out 1’ response of the DC and the ‘Out 1’ response of MZI A. Those responses are shown in Figure 5.9, where the arrow indicates the intersection of the ‘Upper Branch’ and ‘Lower’ responses. The ‘Lower Branch’ response is obtained by multiplication of the complements of the responses in Figure 5.9. Note that the ‘Out 2’ response of the DC is equal to its complement.

The individual branch responses in Figure 5.8 are sinusoidal. Their minimum power is 0. Since a DC power divider is used for equal power division their maximum power is 0.5. Furthermore, the individual branch responses are out of phase. Therefore, the ‘Difference Response’ or total response is also sinusoidal where the maximum and minimum are respectively 0.5 and -0.5. Moreover, the ‘Difference Response’ is the most linear around the normalized frequency 0.25.

Table 5.1: Simulation parameters for design of Figure 5.7 (DC power divider and two MZIs)

| Component | Parameter | Symbol | Value |
|-----------|----------------------------------|------------------|-------|
| DC | DC power coupling coefficient | κ_{DC} | 0.5 |
| MZI A | MZI power coupling coefficient 1 | $\kappa_{MZI,1}$ | 0.5 |
| | MZI power coupling coefficient 2 | $\kappa_{MZI,2}$ | 0.5 |
| | MZI free spectral range | FSR_{MZI} | 1 |
| | MZI phase | ϕ_{MZI} | 0 |
| MZI B | MZI power coupling coefficient 1 | $\kappa_{MZI,1}$ | 0.5 |
| | MZI power coupling coefficient 2 | $\kappa_{MZI,2}$ | 0.5 |
| | MZI free spectral range | FSR_{MZI} | 1 |
| | MZI phase | ϕ_{MZI} | 0 |

**Figure 5.8:** Sum Response (a) and Difference Response (b) of design of Figure 5.7 (DC power divider and two MZIs)

The nonlinear behavior is not the key element, since measures as predistortion can be taken to improve the linearity [5]. However, a discussion about predistortion is beyond the scope of this report. The overlap of the branches is more of concern. Since this overlap results in an increase of the average detected optical power, the noise power will increase. The more overlap, the worse the noise performance will be. The ‘Sum Response’ gives an indication of the overlap of the individual branches. In the case of the ideal branch responses in Figure 4.2, the overlap is zero. The ideal ‘Sum Response’ is then zero at the carrier frequency. For the lower frequencies the ‘Sum Response’ is equal to the response of ‘Branch 2’. For the higher frequencies the ‘Sum Response’ is equal to the response of ‘Branch 1’.

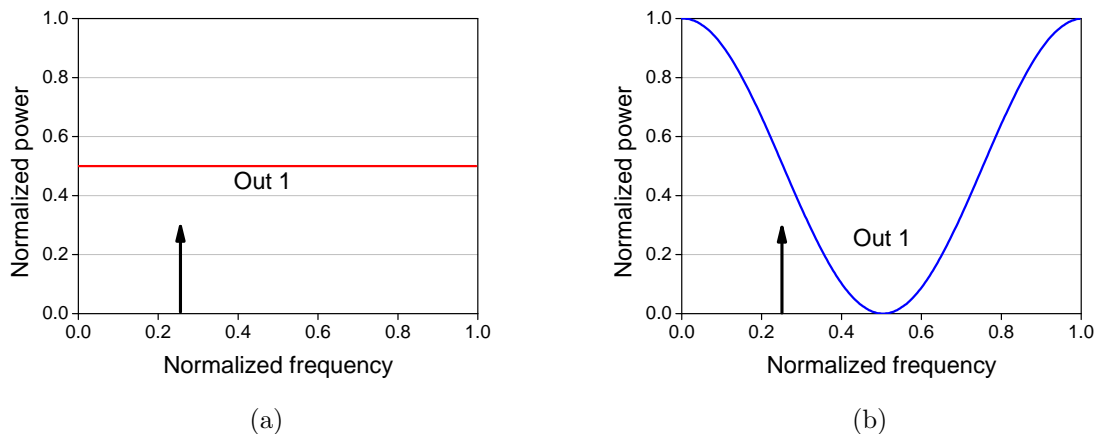


Figure 5.9: (a) 'Out 1' response of the DC and (b) 'Out 1' response of MZI A in Figure 5.7 (DC power divider and two MZIs)

The 'Sum Response' of the simulated design is constant and equal to the maximum power of a single branch (0.5). In other words, since the individual responses do not have the flat parts as required for HWR this design is not suitable for slope detection.

Note that the 'Sum Response' and 'Difference Response' of this design are the same as those of a single MZI, apart from a factor two. The 'Sum Response' and 'Difference Response' of a single MZI can be respectively obtained by addition and subtraction of the responses in Figure 5.5.

5.4.2 DC Power Divider and Two Ring-Resonators

In this design, each DC-output is connected to a ring-resonator as shown in Figure 5.10. The simulation parameters for this design are listed in Table 5.2. The same tuning procedure as in the previous design is used. The FSR is by accident set to 0.5 instead of 1. Since the FSR parameter is normalized and equal for both rings, the choice of its value does not affect the fabrication of the filter. When the rings had different FSR values, only the ratio of these values would be important for the fabrication. To simulate the effect of ring loss, the power loss is set to 0.175 dB per round trip, corresponding to a loss of 0.1 dB/cm for an FSR of 25 GHz.

The simulated responses are shown in Figure 5.4.2. In this figure the 'Upper Branch' corresponds to 'Out 1' and 'Lower Branch' corresponds to 'Out 2'. Consider the 'Upper Branch' response. It is the multiplication of the 'Out 1' response of the DC and the 'Drop' response of Ring A. Those responses are shown in Figure 5.12, where the arrow indicates the intersection of the 'Upper Branch' and 'Lower Branch' responses. The 'Lower Branch' response is obtained in a similar way, but then the 'Drop' response is shifted in frequency.

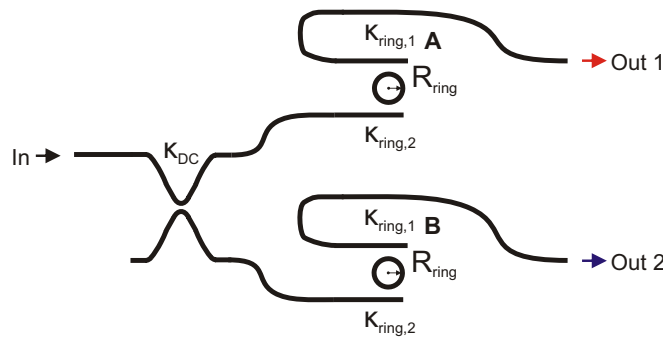


Figure 5.10: Design based on a DC power divider and two ring-resonators

Table 5.2: Simulation parameters for design of Figure 5.10 (DC power divider and two ring-resonators)

| Component | Parameter | Symbol | Value |
|-----------|-----------------------------------|-------------------|------------|
| DC | DC power coupling coefficient | κ_{DC} | 0.5 |
| Ring A | ring power coupling coefficient 1 | $\kappa_{ring,1}$ | 0.33 |
| | ring power coupling coefficient 2 | $\kappa_{ring,2}$ | 0.33 |
| | ring round trip loss | l_{ring} | 0.175 (dB) |
| | ring free spectral range | FSR_{ring} | 0.5 |
| | ring round trip phase | ϕ_{ring} | 0 |
| Ring B | ring power coupling coefficient 1 | $\kappa_{ring,1}$ | 0.33 |
| | ring power coupling coefficient 2 | $\kappa_{ring,2}$ | 0.33 |
| | ring round trip loss | l_{ring} | 0.175 (dB) |
| | ring free spectral range | FSR_{ring} | 0.5 |
| | ring round trip phase | ϕ_{ring} | 1.13 (rad) |

The individual branch responses in Figure 5.4.2 have a Gaussian shape. The individual responses are a better approximation of the ideal branch responses of Figure 4.2 (b) than the individual responses of the MZI-based design of Figure 5.8. As a result, the ‘Sum Response’ is lower around the intersection of the individual branches. However, the overlap of the individual branches is large at the intersection. Furthermore, the ‘Difference Response’ maxima are low. Mainly due to the power splitting by the DC, the normalized maximum and minimum respectively are 0.4 and -0.4.

It is noted that the shape of the individual branch responses are similar to the theoretical responses of a balanced RF-frequency discriminator [9]. In other words, this design is the optical equivalent of the RF-frequency discriminator.

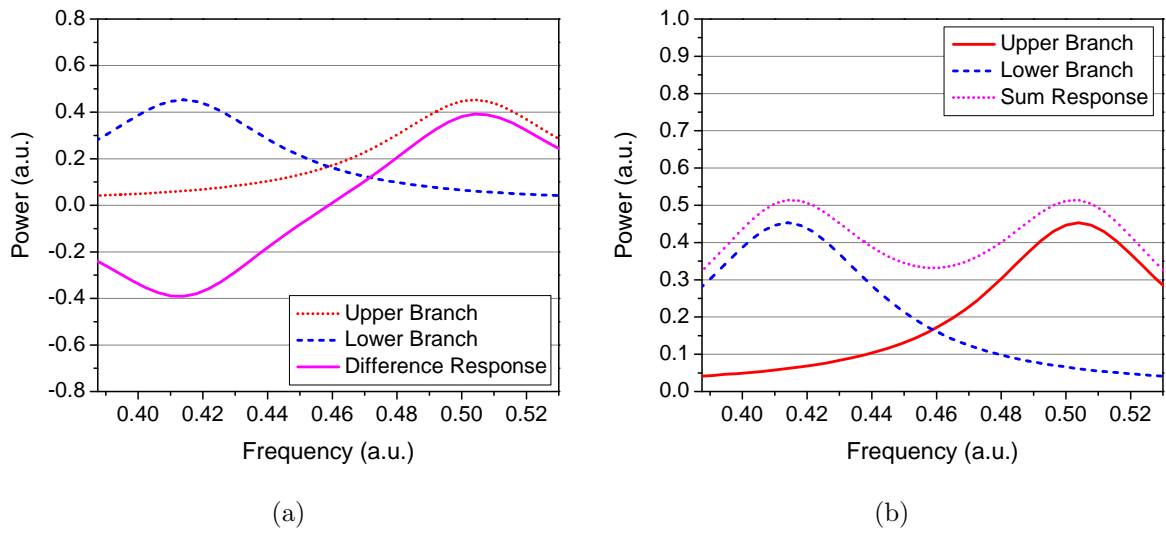


Figure 5.11: Simulated Difference Response (a) and Sum Response (b) of design in Figure 5.10 (DC power divider and two ring-resonators)

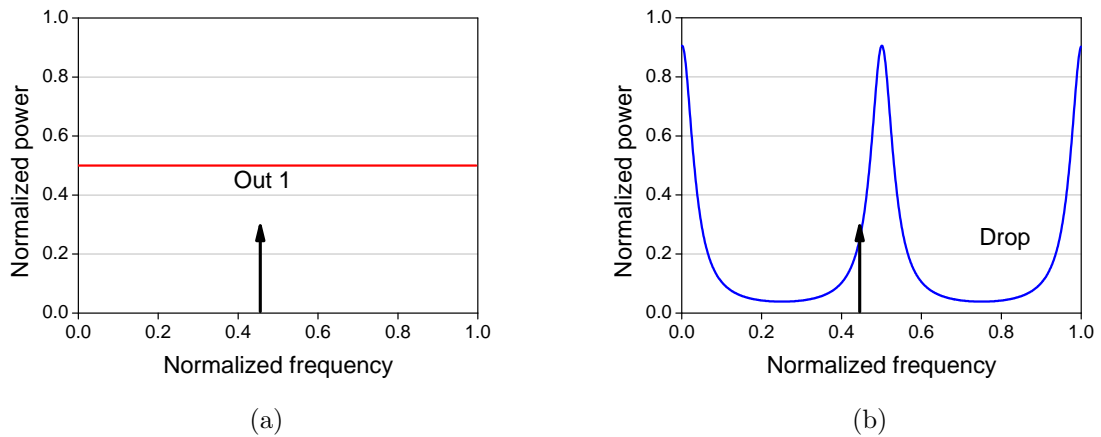


Figure 5.12: (a) 'Out 1' response of the DC and (b) 'Drop' response of Ring A in Figure 5.10 (DC power divider and two ring-resonators)

5.4.3 Three Ring-Resonators

Based on the simulations of two previous designs, a new design is made consisting of three ring-resonators as shown in Figure 5.13.

This design is similar to that of Figure 5.10, but the DC is replaced by a ring-resonator in order to increase the maximum transmission. The simulation parameters for this design are listed in Table B.1 in Appendix B. The simulation results are shown in Figure 5.14.

Consider the 'Upper Branch' response in Figure 5.14. It is the multiplication of the 'Drop' response of Ring A and the 'Through' response of Ring B. Both responses

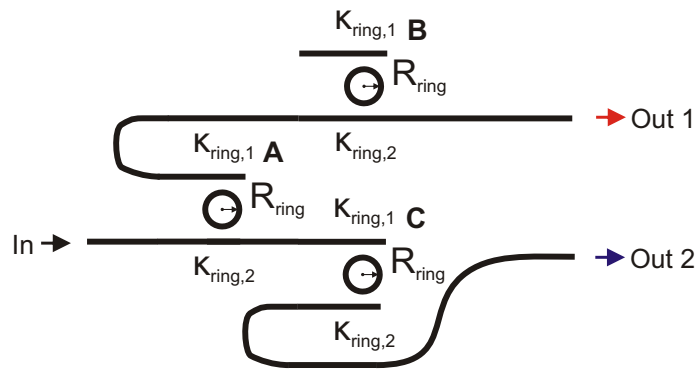


Figure 5.13: Design based on three ring-resonators

are shown in Figure 5.15. The 'Lower Branch' response is obtained by multiplying the 'Through' response of Ring A and the 'Drop' response of Ring C. By properly choosing the settings of Ring C in the 'Lower Branch', the branch responses have shapes which are each other mirror image. The plane of mirror is at the intersection.

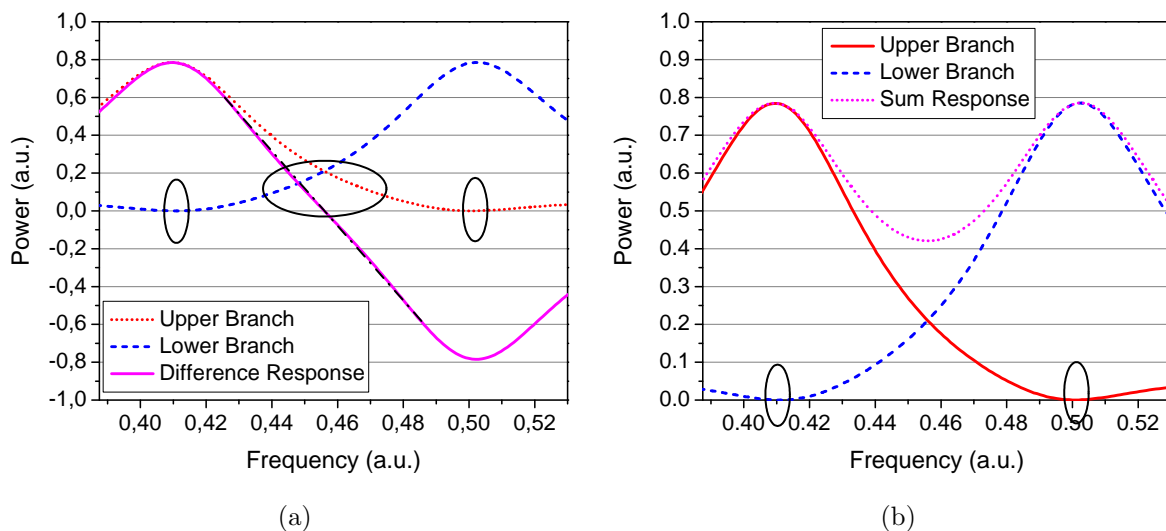


Figure 5.14: Simulated Difference Response (a) and Sum Response (b) of the design in Figure 5.13 (three ring-resonators)

Figure 5.14 shows that the maximum transmission per branch is increased to approximately 0.8. As a result, the 'Difference Response' has 0.8 and -0.8 as maximum and minimum, respectively. Furthermore, the individual branch responses both have a zero, when the complementary branch response is maximum. However, as indicated by the 'Sum Response' there is still an overlap at the intersection of the individual branches.

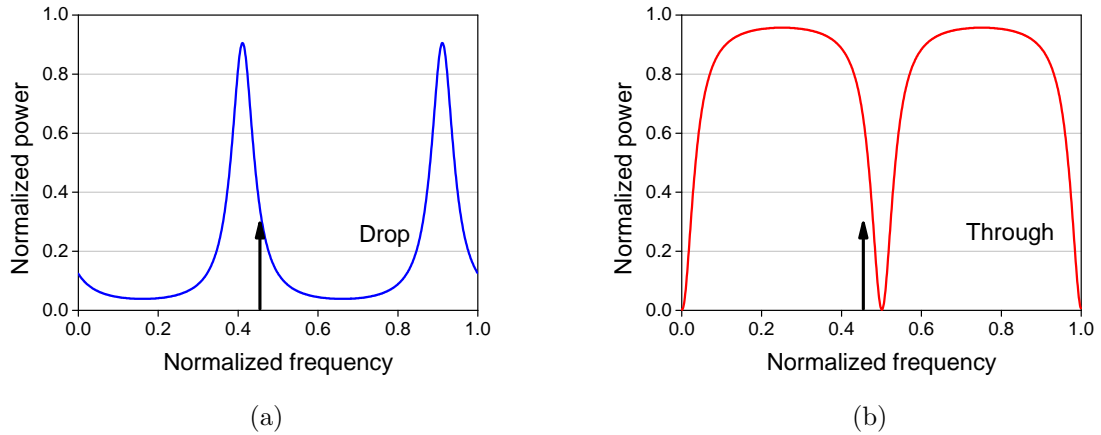


Figure 5.15: (a) 'Drop' response of Ring A and (b) 'Through' response of Ring B in Figure 5.13 (three ring-resonators)

5.4.4 Five Ring-Resonators

The response of the preceding design has a large overlap, which can be reduced by adding zeros in the responses. This is realized by adding a bar coupled ring-resonator in both branches as is shown in Figure 5.16. The zero in each branch response is placed close to the intersection of both branch responses, where in the ideal case will be the transition from the flat to linear part. Besides reducing the overlap, the part which has to carry out the FM-to-IM conversion is also lowered, thereby reducing the slope. By making the FSR of the added rings smaller, the frequency band impacted by the zero is reduced. The FSR of the added rings is set equal to half times the FSR of the other rings. The FSR of the added rings is then still larger than the interesting range for frequency discrimination. In other words, we do not have to bother about an extra zero besides the desired added zero in the frequency range of the frequency discriminator. As a result, the part which has to carry out the FM-to-IM conversion is less lowered than in the case of no halving of FSR. Moreover, there is still a reduction in the overlap.

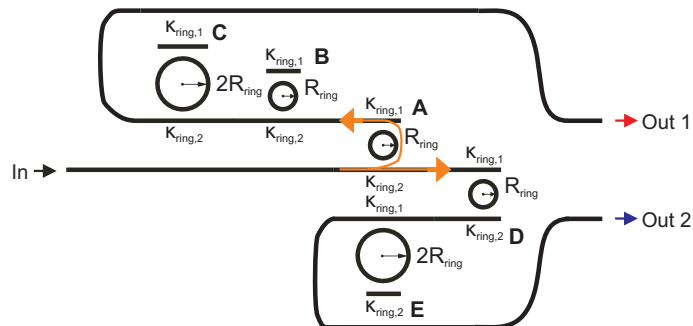


Figure 5.16: Design based on five ring-resonators

The simulation parameters for this design are listed in Tables B.2 and B.3 in Appendix B. The simulation results are shown in Figure 5.17. Consider the ‘Upper Branch’ response in this figure. It is the multiplication of the ‘Drop’ response of Ring A and the ‘Through’ responses of Ring B and C. The ‘Drop’ and ‘Through’ responses of respectively Ring A and Ring B are the same as in Figures 5.15(a) and 5.15(b). Furthermore, the ‘Through’ response of Ring C is shown in Figure 5.18.

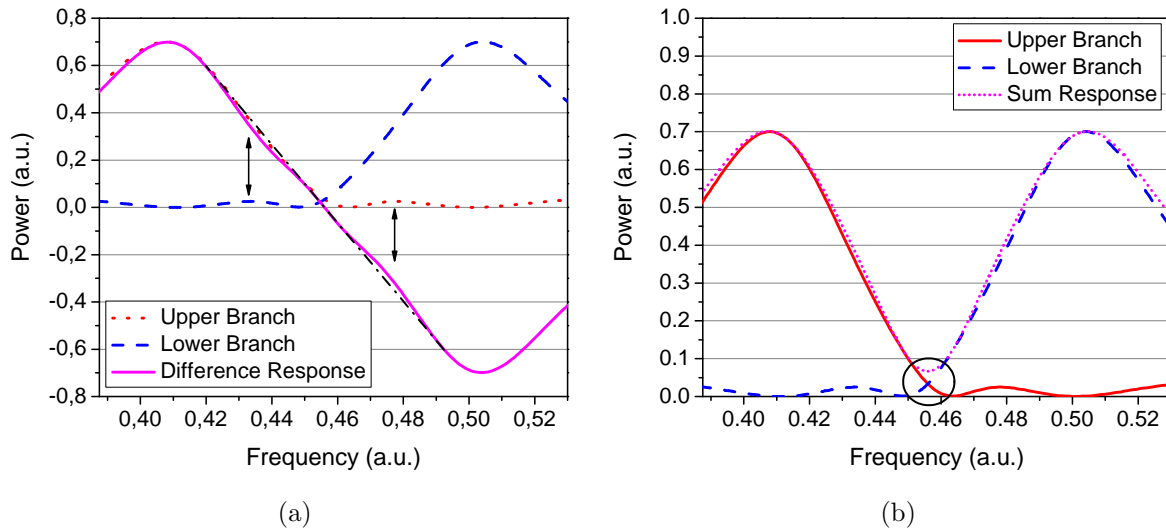


Figure 5.17: Simulated Difference (a) and Sum Response (b) of the design in Figure 5.16 (five ring-resonators)

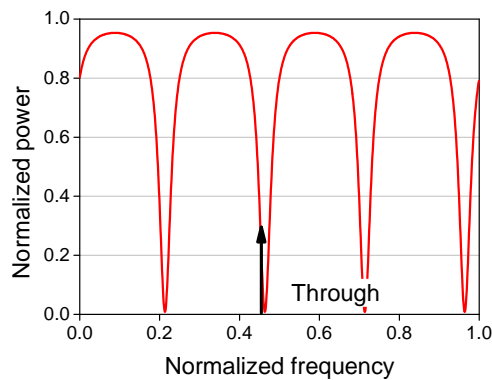


Figure 5.18: ‘Through’ response of Ring C in Figure 5.16 (five ring-resonators)

In Figure 5.16 the number of cross couplings and bar couplings are equal per branch. By properly choosing the settings of the unshared rings in the ‘Lower Branch’, the branch responses have shapes which are each other mirror image. The plane of mirror is at the intersection of the responses.

Figure 5.17 shows that the maximum transmission of each branch response is reduced by 0.1 to 0.7, respectively resulting in 0.7 and -0.7 as maximum and minimum

of the 'Difference Response'. Furthermore, the 'Difference Response' has an increase in nonlinearities. For the purpose of comparison, a dashed straight line is drawn in Figures 5.14(a) and 5.17(a). However, the overlap is indeed reduced.

When adding another ring-resonator in both branches, the residual overlap can be further reduced. Besides, the 'Difference Response' becomes more linear, since the residual overlap gives rise to the nonlinearities in the 'Difference Response', as is indicated in Figure 5.17(a). However, the addition of these extra ring-resonators goes beyond the scope of this report.

Measurements

In this chapter the measurements of the laser FM-characteristics are discussed. Since it is not possible to fabricate the designed filter of the preceding chapter in the project, DWDM-filters are used instead. They are employed in such a way that the concept of the FM-slope detection AOL can be tested.

Before verifying the concept, the laser P-I curve is determined, giving the relation between optical power and laser bias current. Next, the temperature and current dependences of the laser wavelength are determined for the purpose of tuning. Since the DWDM-filters are not tunable, the laser wavelength is tuned. Furthermore, the DWDM-filter transfer is measured by varying the laser wavelength. Using this DWDM-filter transfer, the FM-characteristics are determined. Moreover, the feasibility of the HWR is determined

6.1 Semiconductor Laser Diode P-I Curve

6.1.1 Measurement Setup

The relation between optical power and bias current is measured using the setup in Figure 6.1. The used laser is from Eudyna and its characteristics as specified by the manufacturer are listed in Tabel 6.1. The laser is mounted on an ILX LDM

Table 6.1: Eudyna SLD characteristics

| Parameter | Value | Unit |
|----------------------------|------------------|------|
| Type | FLD5F15CX J9310F | - |
| Wavelength (T: 20 - 35 °C) | 1552.52 | nm |
| Maximum current | 150 | mA |
| Maximum power (minimum) | 10.0 | mW |

laser diode mounting device, which is connected to the ILX Lightwave LDC 3724 SLD

controller. Using this controller, the bias current is varied in the range from 1 to 140 mA and the laser ambient temperature is kept constant at 25.01 °C. The optical power is detected by an optical head which is connected to the power meter. The optical head has a maximum optical input power of 3 dBm. Therefore, the optical power of the laser is attenuated by a variable optical attenuator (VOA) before detection. The important characteristics and settings of the VOA and power meter are listed in Tabel 6.2.

Table 6.2: Characteristics and settings of the VOA and power meter in Figure 6.1

| Device | Parameter | Value | Unit |
|-------------|---------------------|----------------|------|
| VOA | Type | HP 8157A | - |
| | Wavelength | 1552 | nm |
| | Attenuation | See Figure 6.2 | - |
| | Insertion loss | 2.35 | dB |
| Power meter | Type optical head | HP 81521B | - |
| | Type meter | HP 8152A | - |
| | Wavelength | 1552 | nm |
| | Maximum input power | 3 | dBm |

6.1.2 Measurement Results

The measurement results for an attenuation of 10 and 20 dB are shown in Figure 6.2, where the optical power is the calculated power after correction for the VOA attenuation. The inset shows the P-I curves around threshold in more detail. From this inset can be determined that the threshold current of the laser is 11 mA. Furthermore, calculating the slope using the bias currents of 12 and 20 mA and the corresponding optical power, one obtains a slope efficiency s_1 of 0.19 W/A for both curves.

A line with the calculated slope going through the threshold point is plotted in the main graph. From the plotted line can be observed that the relation between optical power and bias current is not linear for both curves. The ‘10 dB attenuation’ curve starts deviating from the straight line around a bias current of 90 mA. Furthermore, the ‘20 dB attenuation’ curve starts deviating from the straight line around 80 mA. In the ‘20 dB attenuation’ measurements the maximum detected optical power is 0.23 mW corresponding to -6.38 dBm, roughly 10 dB below the optical head maximum input power. In other words, the optical head is not saturated for a laser bias current of 80 mA in the ‘20 dB attenuation’ measurements. Therefore, it can be concluded that the nonlinear behavior is a laser characteristic. The difference of 10 mA in the starting points of the deviation is probably due to a measurement inaccuracy, since a gap of 0.5 mW appears between both curves at the end of the measurement range (140 mA) in the main graph.

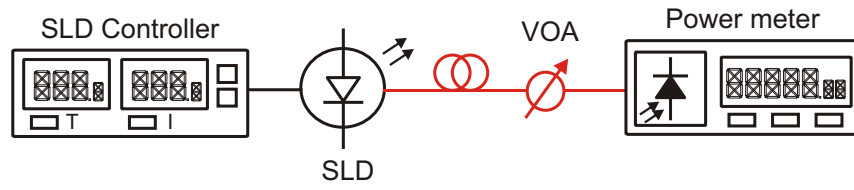


Figure 6.1: Setup for SLD P-I measurement

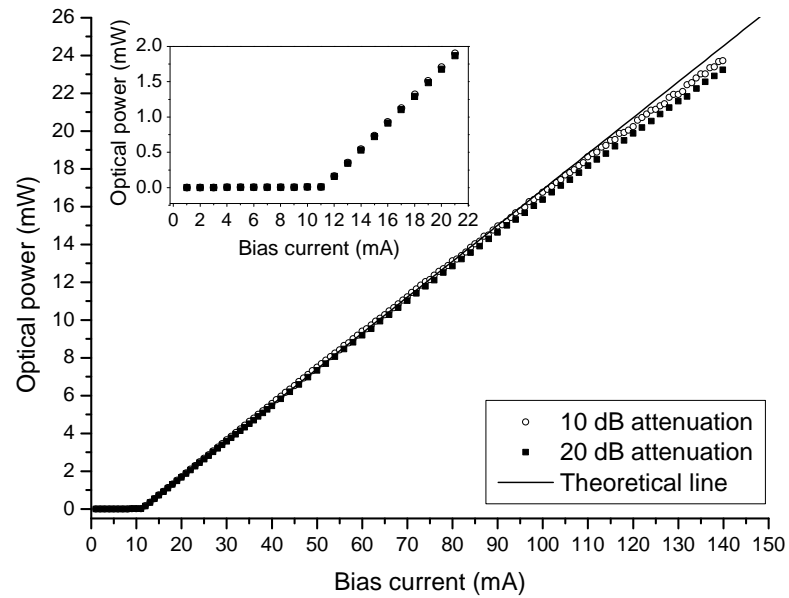


Figure 6.2: SLD P-I curve

6.2 Temperature and Current Dependences of SLD Wavelength

6.2.1 Measurement Setup

The temperature dependencies of the Eudyna SLD wavelength are determined using the measurement setup of Figure 6.3. Again, the laser is mounted on an ILX LDM laser diode mounting device. Using the SLD controller, the laser temperature and laser current are both varied. The temperature is varied in the range from 20.0 to 33.0 °C with steps of 0.5 °C and the current is varied in the range from 15 to 140 mA with steps of 5 mA. The wavelength of the laser is measured by the HP 70951A optical spectrum analyzer (OSA) of which the settings are listed in Table 6.3.

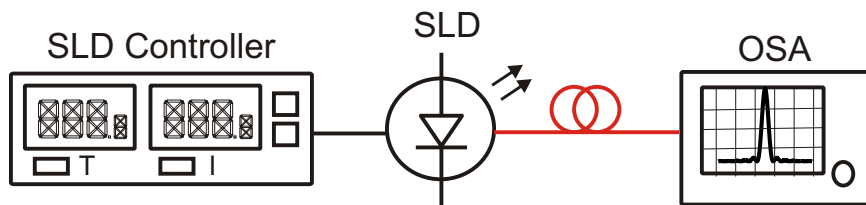


Figure 6.3: Experimental setup for characterization temperature and current sensitivity of SLD-wavelength

Table 6.3: Settings optical spectrum analyzer in Figure 6.3

| Parameter | Value | Unit |
|----------------------|----------|--------|
| Reference level | 30.00 | dBm |
| Sensitivity | -41 | dBm |
| Display scale | 10.00 | dB/div |
| Resolution bandwidth | 0.1 | nm |
| Video bandwidth | 1 | kHz |
| Sweptime | 50 | msec |
| Center wavelength | 1552.000 | nm |
| Span | 3.500 | nm |

6.2.2 Measurement Results

The measurement results are shown in Figure 6.4. The OSA has an absolute accuracy of ± 1 nm. Besides, it took a long time before the setup was stabilized after changing the temperature or current and furthermore the stabilization times were random, requiring user interaction during the measurements. Therefore, the measurements took more

than a day. As a consequence, the absolute accuracy of the OSA becomes observable as gaps between curves and overlapping of curves. However, the tendencies are observable.

As is shown in Figure 6.4 the wavelength is a nonlinear function of the bias current. For every temperature setting, the wavelength changes monotone over the range from 15 mA to 140 mA with the average total change of 0.356 nm corresponding to 44.5 GHz. Furthermore, the wavelength is a linear function of temperature, as is shown in Figure 6.5 for a bias current of 75 mA. The average increase in wavelength for an increase of 0.5 °C for a fixed bias current is calculated. In this calculation the temperature ranges from 20.0 to 24.0 °C, 24.5 to 28.5 °C and 32.0 to 33.0 °C are considered. That are the ranges which are free of gaps and overlaps. The measurement data for the currents 15 mA and 140 mA of the first temperature range are listed in Table 6.4 for the purpose of illustration. The calculated result is 0.055 nm per 0.5 °C, resulting in an average temperature sensitivity of 0.11 nm/°C (corresponding to 13.7 GHz/°C).

Since the wavelength is more sensitive in temperature than in current, the temperature is used as wavelength tuning parameter.

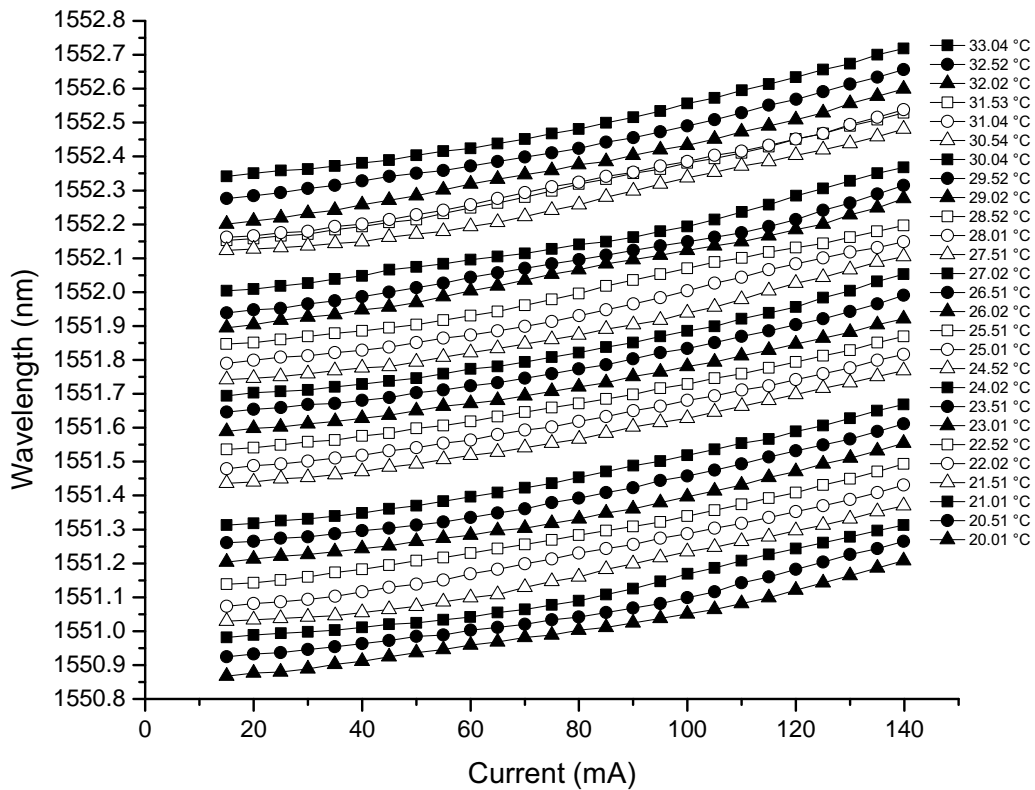


Figure 6.4: SLD wavelength characteristics

Table 6.4: Measurement data for the bias currents 15 mA and 140 mA for determining the wavelength temperature dependence

| I (mA) | T (°C) | λ (nm) | I (mA) | T (°C) | λ (nm) |
|--------|--------|----------------|--------|--------|----------------|
| 15.01 | 20.01 | 1550.867 | 139.87 | 20.01 | 1551.208 |
| | 20.51 | 1550.924 | | 20.51 | 1551.265 |
| | 21.01 | 1550.981 | | 21.01 | 1551.313 |
| | 21.51 | 1551.029 | | 21.51 | 1551.370 |
| | 22.02 | 1551.073 | | 22.02 | 1551.431 |
| | 22.52 | 1551.138 | | 22.52 | 1551.493 |
| | 23.01 | 1551.204 | | 23.01 | 1551.554 |
| | 23.51 | 1551.261 | | 23.51 | 1551.611 |
| | 24.02 | 1551.313 | | 24.02 | 1551.668 |

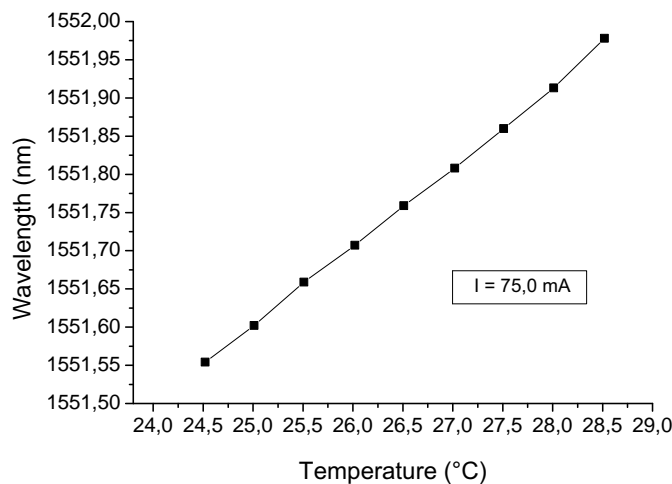


Figure 6.5: SLD wavelength versus temperature

6.3 DWDM Filter Transfer and SLD FM Response

6.3.1 Measurement Setup

Since the laser has an IM-response besides the FM-response, the IM-response must be known in order to determine the FM-response. The IM-response and the FM-response are measured using the measurement setup of Figure 6.6. A network analyzer (NA) provides the modulating RF-signal to the SLD. Then, the optical signal of the laser is equally divided over two branches, an upper and a lower branch. The upper branch is used as reference and is therefore denoted as reference link. It consists of a variable optical attenuator, VOA 1, which tracks the DWDM-filter loss. In this way, the reference link tracks the curve of the DWDM-filter. Furthermore, the attenuator enables

blocking of the reference link. The lower branch consists of the DWDM-filter and is therefore denoted as DWDM-link. This link also has a variable optical attenuator, VOA 2. The attenuator is to prevent the optical power to exceed the detector optical power limit and to enable blocking of the link. The BPD detects one of the links or both links, depending on the settings of the VOAs. The bias-T blocks the DC components in the path to the NA. Furthermore, the DC-output of the bias-T is connected to a multimeter to measure the BPD dc-current.

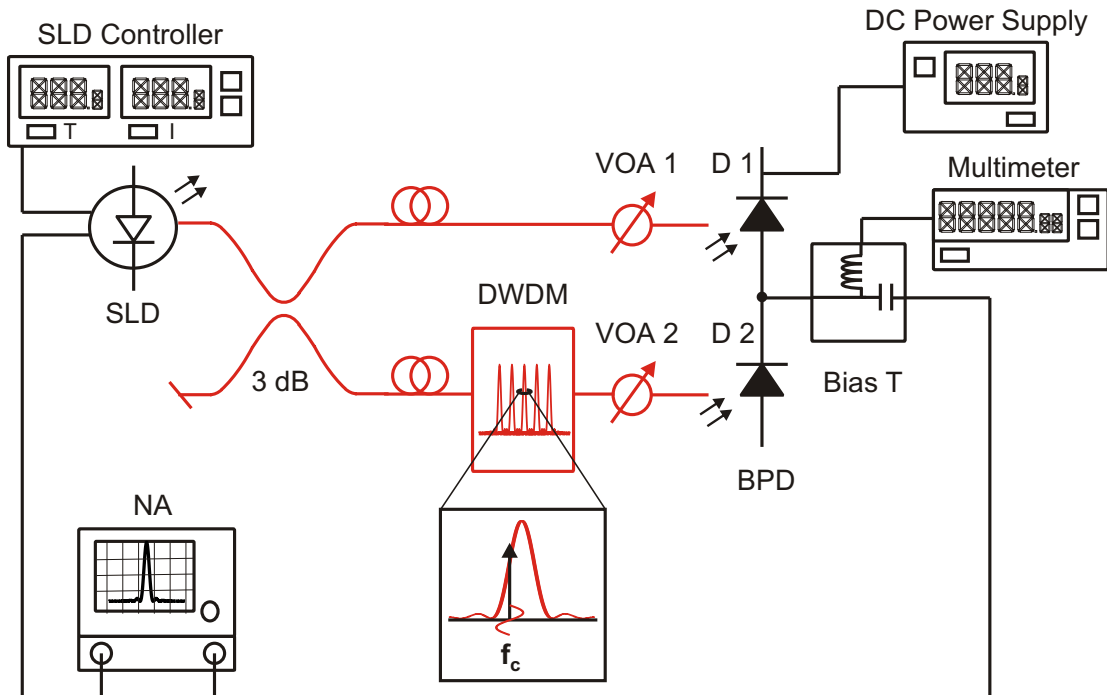


Figure 6.6: Measurement setup for determining the laser FM-characteristics

The measurement procedure starts by setting the temperature and current of the SLD. Next, the DWDM-link is operated in CW-mode and the detected dc-current is measured. Subsequently, both links are operated in CW-mode for tuning the attenuation of the reference link. It is tuned such that the dc-current of the BPD is zero. This results in equal laser IM-responses in both links when measuring the responses of the links. Then, the laser IM-response passing through the DWDM-link is measured by blocking the DWDM-link and operating the NA in the S_{21} mode. Furthermore, the converted FM-response in addition to the laser IM-response is measured by blocking the reference link and operating the NA in the S_{21} mode. Finally, the laser temperature is set to the next value in order to change the laser wavelength and the procedure is repeated. During the measurements the laser current is not changed.

The used SLD, its mounting device and its controller in the setup of Figure 6.6 are the same as in the previous measurements. The laser bias current is set to 75.00 mA, such that the optical power after power splitting does not exceed the maximum optical

input power of a single photodetector (10 dBm). The steps in temperature are 0.1 °C and the range depends on the measurement, as will be seen later on. The details of the other components are listed in Table 6.5 and the settings of the NA are listed in Table 6.6. Furthermore, two AFOP DWDM-filters are available for the measurements.

Table 6.5: Details of components in measurement setup in Figure 6.6

| Component | Type | Remarks |
|-----------------|---|--|
| NA | Agilent Technologies N5230A PNA-L Network Analyzer | See Table 6.6 |
| VOA 1 | ANDO Optical Variable Attenuator AQ-3105 | Mechanical tuning |
| VOA 2 | Hewlett Packard Optical Attenuator HP 8157A | See Table 6.2, attenuation: set to 3.00 dB |
| BPD | Discovery Semiconductors Balanced Photodetector DSC710 | R_{pd} D 1: 0.64 A/W R_{pd} D 2: 0.69 A/W |
| DC power supply | BSI PSM 3/2A 3CH Multi Channels High Performance Regulated DC Power Supply | Channel 1: set to 10.0 V |
| Bias T | Ortel Corporation BN-2 100 kHz - 11 GHz | - |
| Multimeter | Hewlett Packard Multimeter HP34401A | DC-current mode |

Table 6.6: Settings of network analyzer in measurement setup in Figure 6.6

| Parameter | Value | Unit |
|------------------|---------|--------|
| Output power | 10.000 | dBm |
| Reference level | -48.00 | dBm |
| Display scale | 10.00 | dB/div |
| Start frequency | 10.0000 | MHz |
| Stop frequency | 4.00000 | GHz |
| Sweptime | 100.000 | msec |
| Sweep bandwidth | 50.0 | kHz |
| Sweep type | linear | - |
| Number of points | 1024 | - |
| Averaging | off | - |

6.3.2 Measurement Results

Channel Transfer and Reference Responses

First of all, the filter transfer is determined in order to determine the interesting temperature ranges for the response measurements of the reference link and DWDM-link. The

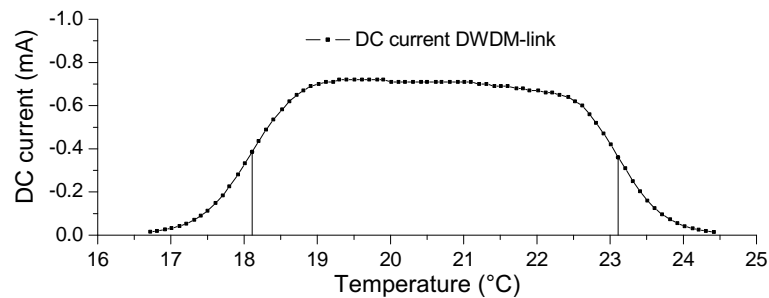


Figure 6.7: Measured dc-current of Channel 32 of DWDM 1

filter transfer is determined by measuring the detected dc-current of the DWDM-link in the absence of the modulation signal. Note that this current is linear proportional to the detected optical power. Figure 6.7 shows the measurement results for channel 32 of DWDM 1. In this figure the current as function of temperature is plotted. The interesting range for the measurements are around the temperatures of 18.11 °C and 23.11 °C. The temperatures of 18.11 °C and 23.11 °C, indicated by a drop line, are the optical 3 dB points of the filter. Since the slopes are large at these points, the FM-to-IM conversion efficiency is expected to be large at these points.

In order to determine the FM response, the measured reference link response is subtracted from the measured DWDM-link response. Therefore, the relation between the filter transfer and reference link response is discussed before the actual discussion of the measurement results. The reference responses corresponding to the previous discussed filter transfer are shown in Figure 6.8. A logarithmic as well as a linear plot for eight RF frequencies are shown. As can be seen, all the reference response neatly tracks the filter transfer. In the linear plot the reference responses are decreasing in the passband region, as a result of the not fully flat passband. Moreover, from the logarithmic plot can be determined that the responses are within 6 dB to each other. This indicates that the frequency band from 0.50 to 4.0 GHz is within the 3 dB optical bandwidth of the modulation device in case of IM.

FM responses

For the measurements on Channel 32 of DWDM 1, the temperature is varied in the range from 16.7 to 24.4 °C. The S_{21} measurement results of both links are shown in Figure 6.9 for eight temperature settings. The selection of temperatures is based on the probed position of the channel transfer. The response curves corresponding to same channel transfer loss or average detected optical power have the same line style and color. In the figure the measure for average detected optical power, in the absence of modulation signal, is the detected dc-current. For example, the reference link response and corresponding DWDM-link response measured at a temperature of 18.62 °C have

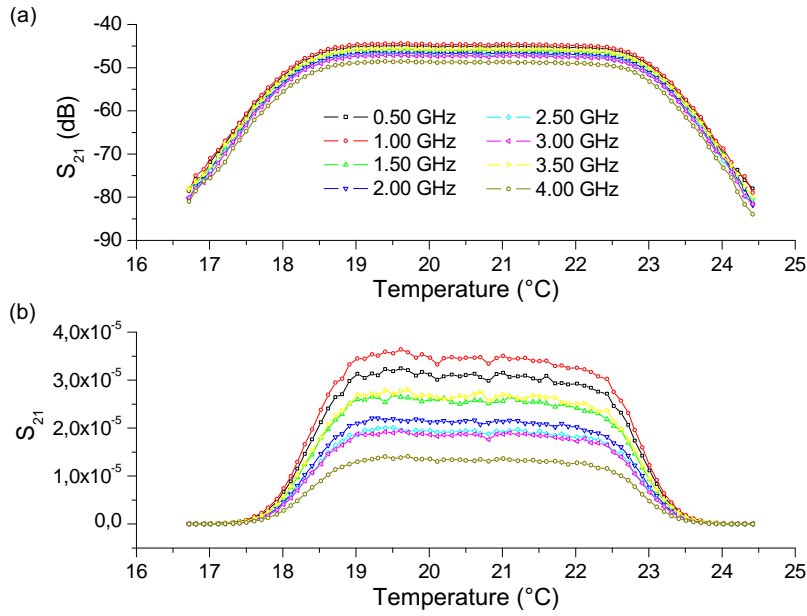
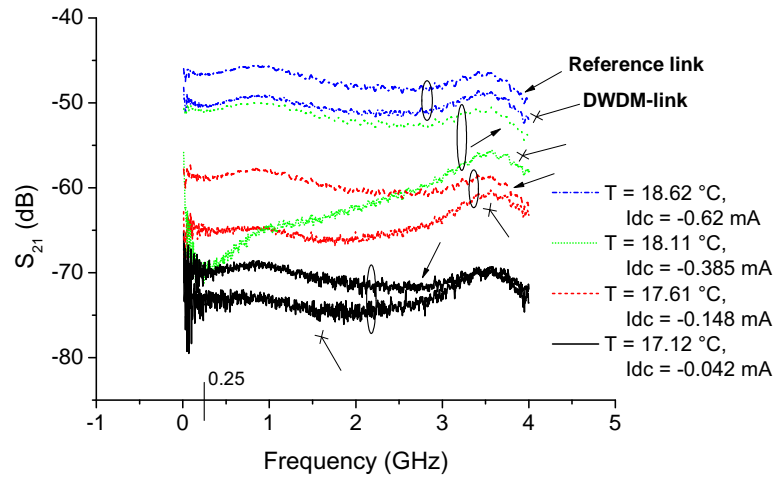


Figure 6.8: IM reference responses for Channel 32 of DWDM 1: (a) logarithmic scale and (b) linear scale

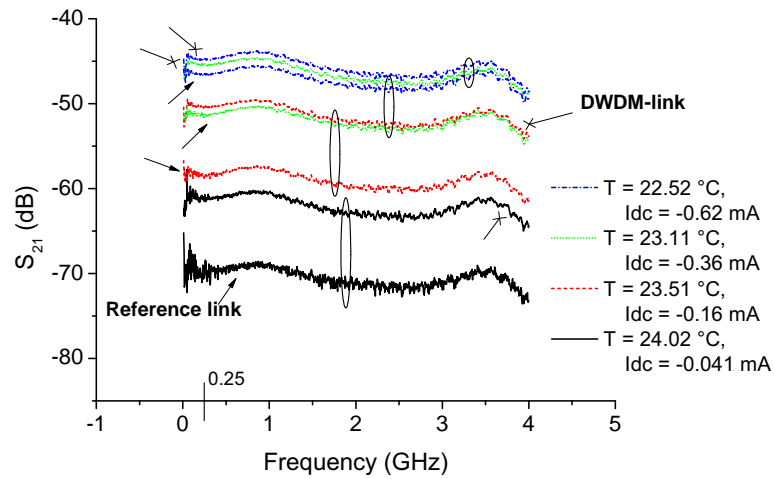
the same style and color. Furthermore, this pair of responses for the positive slope corresponds to those for the negative slope measured at a temperature of 22.52 $^{\circ}\text{C}$.

In Figure 6.9(a) the DWDM-link responses are lower than or almost equal to the reference response. A lower DWDM-link response indicates cancellation of the intensity modulated signal coming from the laser. For example, consider the pair of responses measured at a temperature of 18.11 $^{\circ}\text{C}$. Around the frequency of 0.25 GHz the difference between the two responses is roughly 20 dB. This means that the intensity modulated signal generated in the FM-to-IM conversion is almost equal to and out of phase with the intensity modulated signal of the laser. For increasing frequency the distance between the responses decreases. In other words, the contribution of the converted frequency modulated signal decreases for increasing frequency. In the cases where the distance between the curves of a pair of responses becomes almost zero, the contribution of the converted frequency modulated signal is negligible.

In Figure 6.9(b) the DWDM link responses are higher than the reference responses. As a result of the changed sign in slope value, the contribution of the converted frequency modulated signal adds to the intensity modulated signal coming from the laser. For example, consider the pair of responses measured at a temperature of 24.02 $^{\circ}\text{C}$. At the frequency of 1.0 GHz the difference between the responses is roughly 10 dB. This means that the converted frequency modulated signal is responsible for the 10 dB increase in the detected signal. In other words, after detection its contribution is approximately 10 times stronger than that of the intensity modulated signal coming from the laser. Although it is not that clearly perceptible as in the negative slope case,



(a)



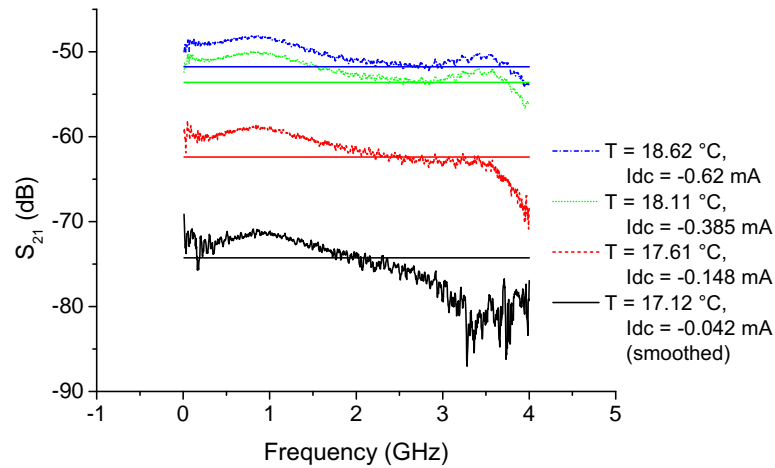
(b)

Figure 6.9: Measurement results DWDM 1 Channel 32: positive slope (a) and negative slope (b)

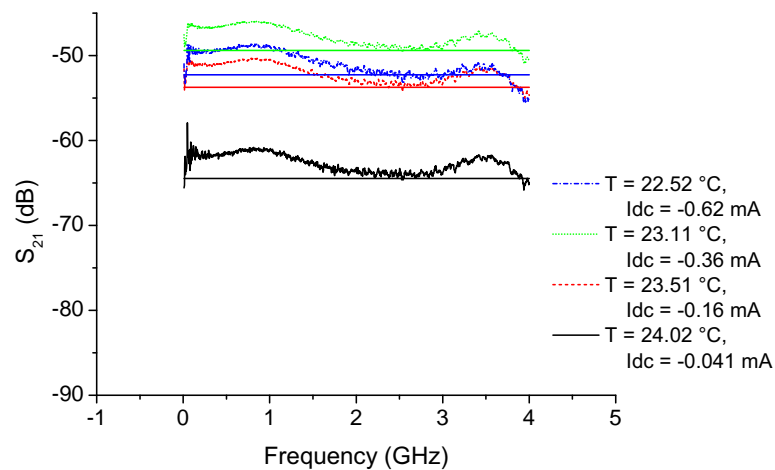
the contribution of the converted frequency modulated signal decreases for increasing frequency.

In Figure 6.10 the calculated FM responses are shown. In the calculation, the measured responses are converted to linear scale first. Then, the DWDM-link response is subtracted from its corresponding reference response. Next, the absolute value of the resulting difference, the calculated FM response, is back-converted to logarithmic scale and plotted. In this figure the same convention concerning the line style and color of the response curves is used as in Figure 6.9. Besides the responses, the -3 dB level for every frequency response is plotted. This level is obtained by taking as

reference the calculated response value for the frequency of 0.50 GHz. It shows that the responses decrease for increasing frequency, as was observed before. Especially, the responses of the positive slope measured at the two lowest temperatures fall off very fast for increasing frequency. The other responses do not have this rapid fall off. It is noted that the calculated FM response for 17.12 °C is very noisy. Therefore, a smoothed version is shown here, which follows the trend of the noisy response.



(a)

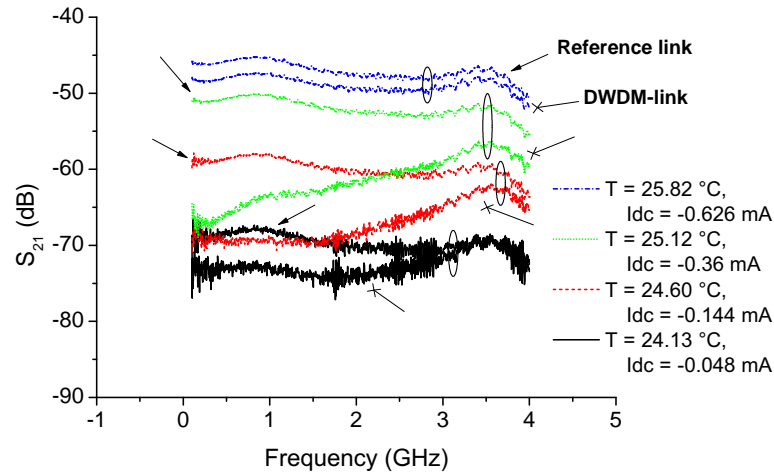


(b)

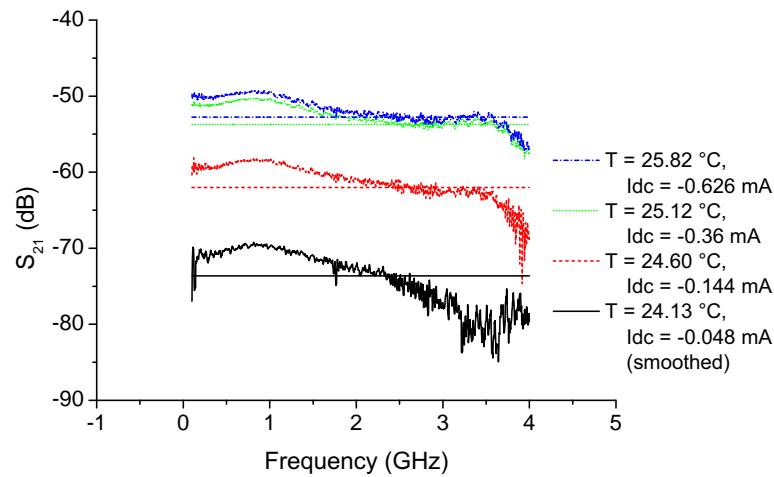
Figure 6.10: Calculated FM response DWDM 1 Channel 32: positive slope (a) and negative slope (b)

In order to further investigate the FM response another measurement is performed on the positive slope of Channel 31 of DWDM 1. The temperature is varied in the range from 23.0 to 27.0 °C and the frequency is swept from 0.1 to 4.0 GHz. The measured

reference link and DWDM-link responses and the calculated FM responses are shown in Figure 6.11 for four different temperature settings. The reference responses as well as the DWDM-link responses are similar to those corresponding to the positive slope of Channel 32 of DWDM 1. All the calculated FM responses show a decreasing response as function of frequency. The lowest response, the response for the temperature of 24.13 °C, is smoothed and has the largest fall off.



(a)



(b)

Figure 6.11: Measured responses (a) and calculated FM response (b) DWDM 1 Channel 31

So far, the measurement results show that there is indeed frequency modulation as result of direct modulation of an SLD. Furthermore, it shows that the contribution of the converted frequency modulated signal decreases for increasing frequency. In order to investigate the effect of modulation depth on the FM, measurements are carried out

in which the RF-power is varied. In these measurements, the optical 3 dB points of the channel transfer of Channel 31 of DWDM 1 and of Channel 32 of DWDM 2 are probed. Since the linearity of the transfer is high around these points, the nonlinear effects of the channel are low. For any difference in the responses as function of RF power, it is presumable that they can be attributed to the modulation device.

Figures 6.12 and 6.13 show the results for the measurements where the RF-power is used as parameter. The results of two different RF-powers are shown. The shape as well as the magnitude of the responses do not change as function of RF-power. The difference in the responses is due to the change in signal-to-noise ratio (SNR). Remember that the average optical power and therefore the noise is the same for both RF-powers. Besides, the calculated FM responses are determined. These responses are shown in Figure 6.14 and do not significantly differ from the calculated responses already discussed in this chapter. Furthermore, the shape as well as the magnitude of the calculated FM responses do not change as function of RF-power. Therefore, the results show the laser chirp is linear dependent on signal current.

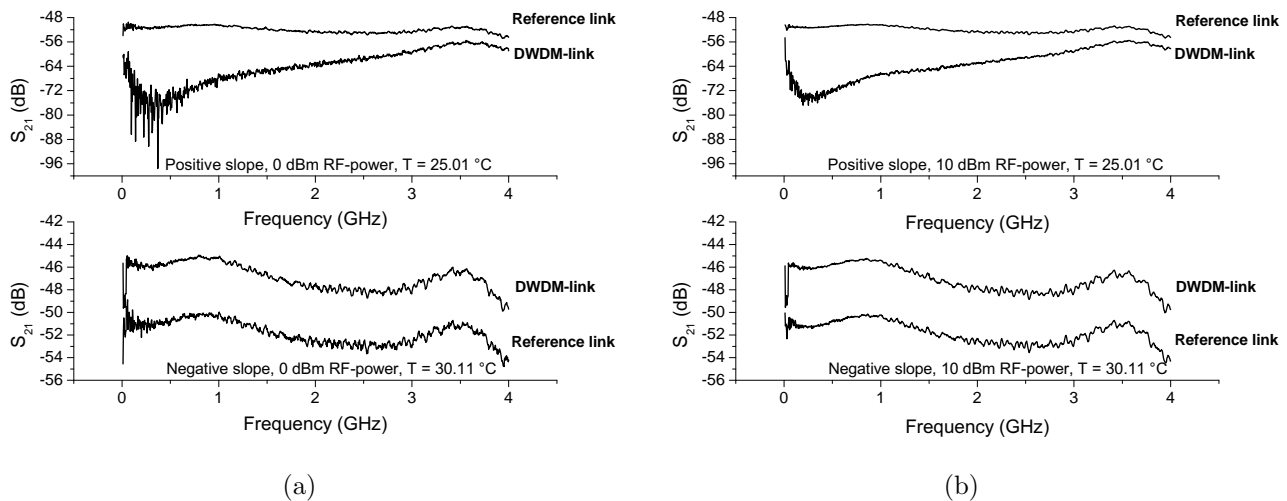


Figure 6.12: Measurement results DWDM 1 Channel 31 for different RF-powers: (a) 0 dBm and (b) 10 dBm

In the most cases we have discussed, the calculated FM responses corresponding to the positive slope are lower than those corresponding to the negative slope. Furthermore, the calculated positive slope FM responses have larger fall off than the calculated negative slope FM responses. However, to compare the responses the effect of the filter transfer must be known. Therefore, the calculated FM responses for Channel 32 of DWDM 1 are plotted as function of temperature in Figure 6.15. Furthermore, the channel transfer function is shown.

First the temperature range corresponding to the negative slope of Channel 32 is considered (Figure 6.15). Starting from the channel passband part, the calculated FM

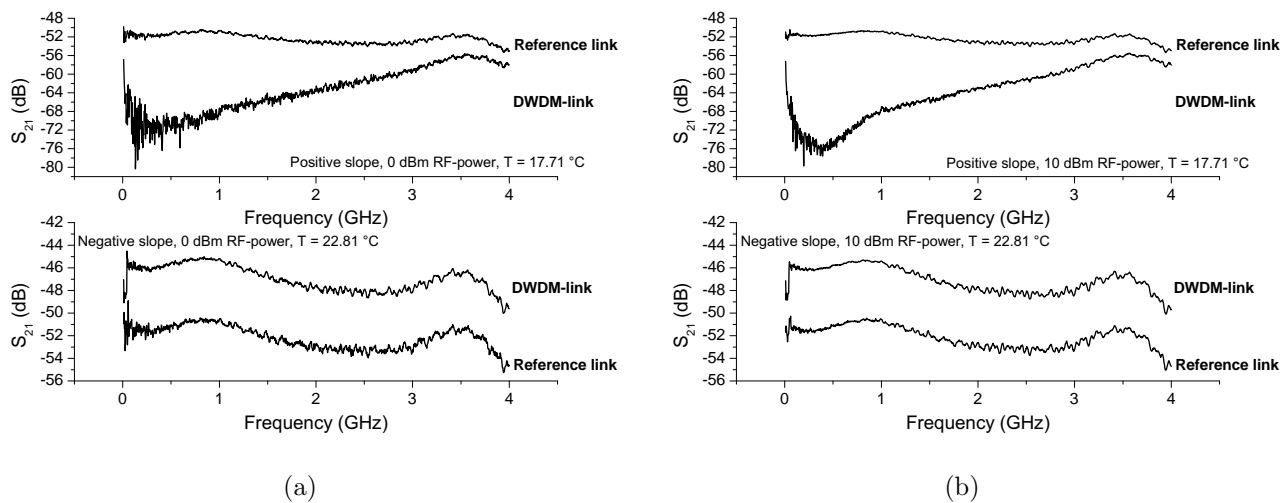


Figure 6.13: Measurement results DWDM 2 Channel 32 for different RF-powers: (a) 0 dBm and (b) 10 dBm

response increases for increasing slope. The maximum of the responses are around the temperature corresponding to the 3 dB point of the channel filter transfer. Subsequently, the FM response decreases for decreasing filter transfer slope. Note that the responses of the different frequencies are close to each other. This agrees with the small decrease, smaller than 2 dB, in frequency responses as observed before.

Next, we consider in Figure 6.15 the temperature range corresponding to the positive slope of the channel. Starting from the channel passband part, the calculated FM responses increases for increasing slope. Their maximum are before the temperature corresponding to the 3 dB point of the channel transfer. Subsequently, the FM responses decrease. Below the temperature of 18.0 °C the response curves become less neatly arranged. Especially, the higher frequency responses fluctuate. It should be noted that below the temperature of 17.4 °C the corresponding DWDM-link responses of the calculated FM responses are very low. Therefore, the DWDM-link responses are affected by noise of the measurement setup. This noise also affects the calculated FM responses. Furthermore, the responses of the higher frequencies are more separated from each other. This agrees with the earlier observed rapid fall off in the frequency responses.

Finally, the less interesting temperature range corresponding to the passband of the channel transfer is considered in Figure 6.15. In theory there is no FM-to IM conversion in an ideal flat passband. Then, the difference between the reference link response and the DWDM-link response is zero. However, the small deviations in the flat channel response results in FM-to-IM conversions. Furthermore, due to inaccuracies during tuning and noise, the laser IM response of the DWDM-link slightly deviates from the measured laser IM response of the reference link. Note that the average optical power

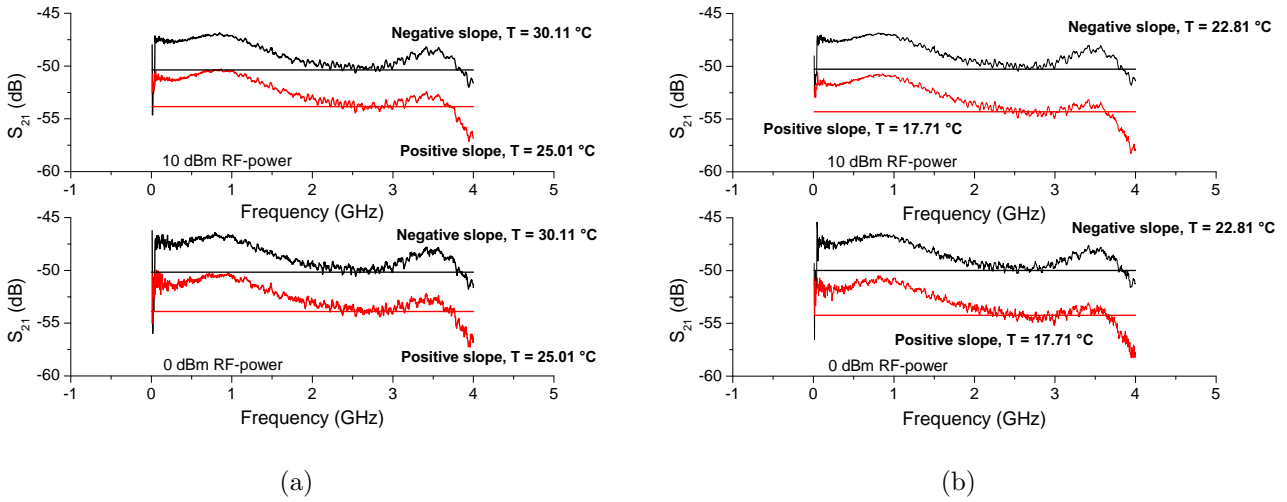


Figure 6.14: Calculated FM responses for different RF powers: DWDM 1 Channel 31 (a) and DWDM 2 Channel 32 (b)

is large in the passband of the channel transfer, resulting in significant optical power related noise. All these will result in a noisy response as shown in the figure.

When considering the channel transfer, we expected that the calculated FM responses would be maximal around the 3 dB points of the channel transfer. Around the -3 dB points the slope of the transfer is large and therefore we expected a large FM-to-IM conversion. However, Figure 6.15 shows that the calculated FM responses do not have their maximum around these points. It must be kept in mind that the laser dynamics per temperature setting can affect the frequency modulation. A conceivable result can be a change in the phase of the converted frequency modulated signal while its intensity is unaffected. In other words, it might be possible that the calculated FM response does not agree with the laser frequency modulation efficiency. In addition, the slope of the channel transfer might have local variations. This will result in a higher or lower slope than expected. Besides, the DWDM filter is dispersive in the transition bands of the channels, which can also affect the measurement results. Therefore, further investigation is needed in order to determine the meaning of the observed behavior of the responses in Figure 6.15.

In order to determine the difference in effect on the measured responses for positive and negative channel transfer slopes, the calculated FM responses around the intersection of two DWDM channels are compared. In Figure 6.16 the calculated responses around the intersection of Channels 31 and 32 are shown. The positive slope responses of Channel 31 show the same behavior as the positive slope responses of Channel 32. The maximum responses are not around the 3 dB point of the channel transfer. Furthermore, the responses are rapidly fluctuating. Moreover, the higher frequency responses are more separated from each other. However, at the intersection the laser

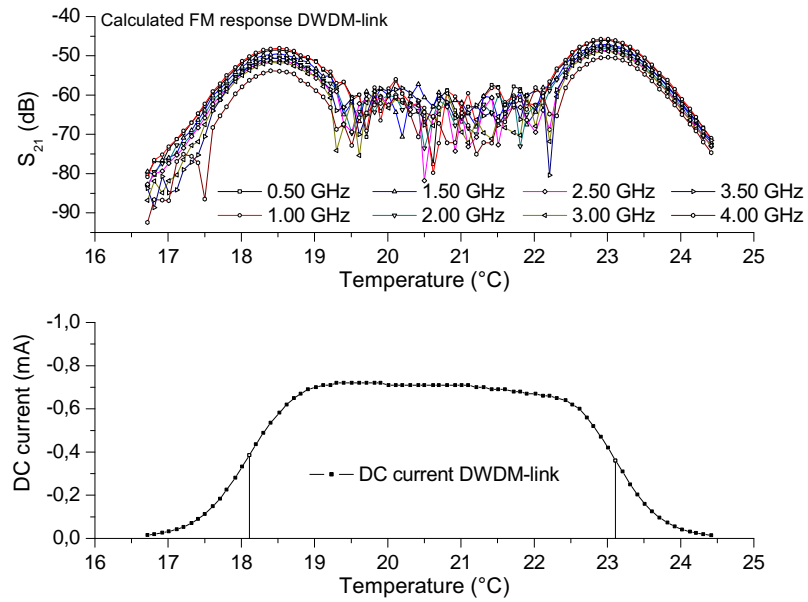


Figure 6.15: Calculated FM responses and transfer Channel 32 DWDM 1

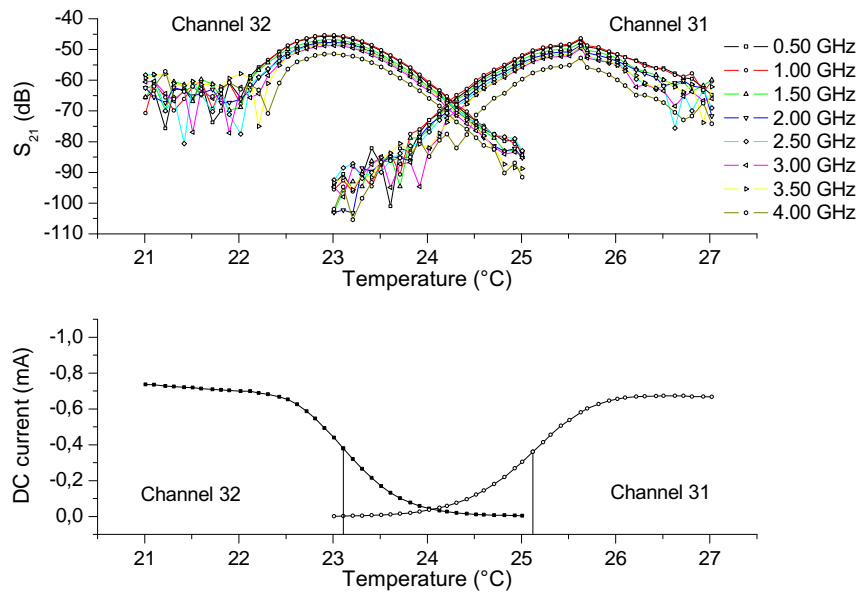


Figure 6.16: Calculated FM responses at intersection of Channels 31 and 32 DWDM 1

temperature settings are the same for both channel transfer slopes. Therefore, the laser dynamics are the same. In other words, at least the DWDM filter is responsible for the different behavior observed for the different slopes.

SLD Chirp Parameter

Despite the characteristics of the FM signal are not fully known, an estimate of the laser chirp parameter can be made. For this, we use the calculated FM response in order to determine the signal current or optical signal power. Furthermore, the channel slope and the average optical power are needed. Table 6.7 gives an overview of the used parameters for determination of the laser chirp parameter. The laser chirp parameter is calculated for the 1 GHz signal measured at the temperature setting of 23.11 °C probing the negative slope of Channel 32 of DWDM 1. The probed point is the 3-dB point of the channel transfer.

The resulting chirp parameter is $1.40 \cdot 10^{-3}$ nm/mW. This corresponds to a laser chirp of 0.175 GHz/mW which is small compared to the results in [7]. In [7] measurements on a heteroepitaxial ridge overgrown distributed feedback laser are discussed. The work shows that chirp parameters in the order of 1 to 60 GHz/mW for a modulation signal bandwidth up to 4.0 GHz are achievable.

Table 6.7: Parameters used for calculation of laser chirp parameter

| Parameter | Value | Unit | Remarks |
|-------------------------------------|----------------------|-------|---------------------------|
| Calculated FM response | -36.1 | dBm | 10 dBm RF power |
| Signal current | $7.01 \cdot 10^{-2}$ | mA | 50 Ω impedance |
| Optical signal power @ detector | $1.02 \cdot 10^{-1}$ | mW | R_{pd} D 2: 0.69 A/W |
| Optical signal power @ DWDM output | $3.48 \cdot 10^{-1}$ | mW | 5.35 dB total loss VOA 2 |
| Detected DC-current @ 23.01 °C | -0.420 | mA | no modulation |
| Detected DC-current @ 23.21 °C | -0.310 | mA | no modulation |
| Slope filter transfer | 0.55 | mA/°C | average @ -23.11 °C |
| Slope filter transfer | 5.0 | mA/nm | no modulation, 0.11 nm/°C |
| Slope filter transfer @ detector | 7.25 | mW/nm | R_{pd} D 2: 0.69 A/W |
| Slope filter transfer @ DWDM output | 24.8 | mW/nm | 5.35 dB total loss VOA 2 |

Half-Wave Rectification

Since the channel transfer slope is changing, the FM-to-IM conversion efficiency is locally changing. Some parts of the converted FM signal wave will be larger than other parts depending on the probed point in the filter transfer. In other words, half-wave rectification (HWR) will occur to some extent. While measuring the DWDM-link

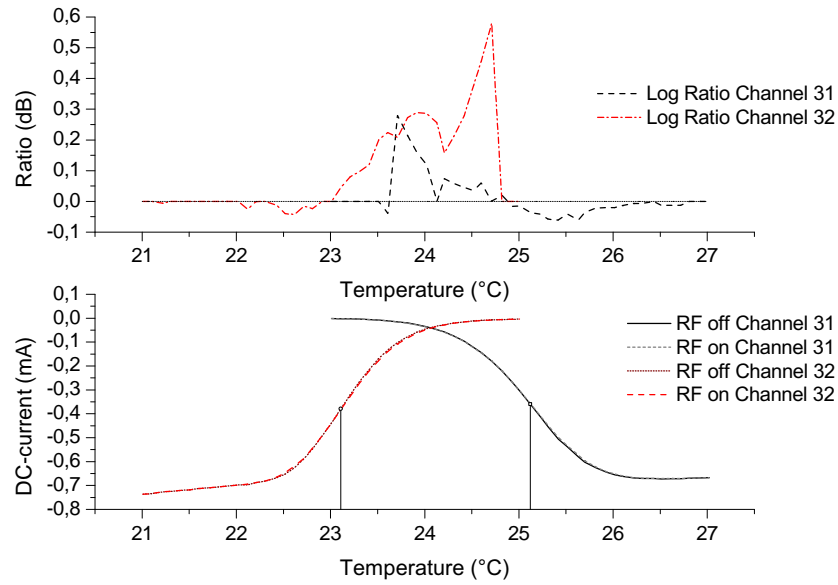


Figure 6.17: Comparison dc-currents in DWDM-link around the intersection of Channels 31 and 32 of DWDM 1

responses for the negative slope of Channel 32 and the positive slope of Channel 31 of DWDM 1, the detected dc-current of the DWDM-link is measured. The dc-current in presence as well as in absence of modulation is measured. A difference between those currents is an indication of HWR. In Figure 6.17 the measured dc-currents are shown. Moreover, the ratio of the measured dc-current in presence of modulation over the measured dc-current in absence of modulation is shown. Besides, a dashed line representing the 0 dB level is shown.

The results in Figure 6.17 show that depending on the change in slope there is a difference between the two measured dc-currents. The sign of this difference changes around the 3 dB points, where the transfer slope value changes sign. Despite the differences are very small, the results show that there is indeed HWR.

Conclusion and Recommendations

In this work, a filter is designed for slope detection in an FM-slope detection AOL. The filter consist of one input and two outputs and its design is based on ring-resonators. In this way the filter can be made tunable resulting in a flexible device. Furthermore, the filter can be integrated in a balanced photodetector (BPD) resulting in a small device.

For half-wave rectification (HWR), the output branches must have a flat suppression band and a linear passband transfer. The transition from the flat to linear transfer must be instantaneous. Besides, the transfers of the individual output branches must be aligned such that the transitions of the individual output branch transfers intersect. Using 5 ring-resonators, a small overlap between the branch output responses is obtained. Furthermore, the transition in the branch response from the suppression band to the pass band are not instantaneous. As a result, there is power leakage around the intersection. Furthermore, the passband transfers are not linear. Moreover, the total response, the response detected by the BPD, has also nonlinearities as a result of the overlaps of the branch responses around the intersection. These effects must be further investigated by simulations and measurements on the fabricated filters.

It can be interesting to investigate the effect of adding zeros to the branch responses to reduce the overlaps around the intersection. The addition of zeros can be realized by adding a bar coupled ring to each individual branch. Furthermore, it is interesting to investigate the possibilities of predistortion techniques. Those techniques can be used for compensation of nonlinearities.

In the filter design it is assumed that the laser intensity modulation (IM) is negligible compared to the converted frequency modulation (FM). When the filter is fabricated this assumption must be checked on its validity. If it turns out that the assumption is invalid, one can redesign the filter to enlarge the slope in the branch transfers. In this way the desired FM-to-IM conversion can be enlarged. So far we know, there are no optical power limiters available to suppress the laser IM. Therefore, it is quite interesting to investigate if components such as optical amplifiers can be

used as intensity limiters.

The measurement setup used for characterization of the laser chirp incorporates a DWDM-filter as slope detector. However, the influence of the DWDM-filter on the converted frequency modulated signal is not fully determined. To determine the effect, measurements employing an optical phase modulator can be carried out to characterize the DWDM-filter. However, one effect of the DWDM-filter is already determined. The observed large fall-off in frequency responses for the probed points at the positive slope is at least due to the filter. Another disadvantage is that the measurement method is based on interference with the laser intensity modulated signal. As a result, it can not be distinguished between a phase shift or reduction in optical power of the converted frequency modulated signal. A solution for this problem can be the application of the alternative measurement setups discussed in [10]. Among others, techniques measuring the modulation side bands in the optical spectrum are treated in [10].

Despite the advantages of the measurement setup, we can conclude that there is indeed frequency modulation. Furthermore, a linear dependence of the laser chirp, or instantaneous frequency deviation, on the instantaneous modulation signal current is shown. Besides, a weak form of HWR is shown. Moreover, an estimated of the laser parameter is given. Its value (0.175 GHz/mW for an 1.0 GHz RF-frequency) is small, but that can be a consequence of the used measurement method.

References

- [1] D.A.I. Marpaung, C.G.H. Roeloffzen and W. van Etten "Dynamic Range Enhancement in Analog Optical Links with a Balanced Modulation and Detection Scheme", *Proceedings of the International Topical Meeting on Microwave Photonics (MWP'2006)*, Grenoble, France, 3-6 October 2006, p. P10.
- [2] D.A.I. Marpaung, C.G.H. Roeloffzen and W. van Etten "A novel modulation scheme for noise reduction in analog fiber optic links", *Proc. of the 10th IEEE/LEOS Symp. in the Benelux*, Mons, Belgium, December 2005, pp. 113-116.
- [3] T.E. Darcie, J. Zhang, P.F. Driessen and J.J. Eun "Class-B Microwave-Photonic Link Using Optical Frequency Modulation and Linear Frequency Discriminators", *Journal of Lightwave Technology*, vol. 25, no. 1, pp. 157-164, 2007.
- [4] J. Zhang, A.N. Hone, T.E. Darcie "Limitation Due to Signal-Clipping in Linearized Microwave-Photonic Links", *IEEE Photonics Technology Letters*, vol. 19, no. 14, pp. 1033-1035, 2007.
- [5] Cox, Charles H. III: *Analog Optical Links* (2004), Cambridge University Press, Cambridge (UK), 288 p.
- [6] Marpaung, D.A.I. and Roeloffzen, C.G.H. and van Etten, W.C. "Characterization of a Balanced Modulation and Detection Analog Optical Link", 12th Annual Symposium IEEE/LEOS Benelux, 17-18 Dec 2007, Brussels, Belgium. pp. 255-258.
- [7] T.L. Koch and J.E. Bowers "Nature of wavelength chirping in directly modulated semiconductor lasers", *Electronics Letters*, vol. 20, no. 25, pp. 1038-1040, 1984.
- [8] C.K. Madsen and J.H. Zhao: *Optical Filter Design and Analysis: A Signal Processing Approach* (1999), John Wiley & Sons, Inc., New York (USA), 432 p.
- [9] Haykin, Simon S.: *An Introduction to Analog and Digital Communications* (1989), John Wiley & Sons, Inc., New York (USA), 652 p.
- [10] L. Bjerkan, A. Rgyset, L. Hafskjaer and D. Myhre "Measurement of Laser Parameters for Simulation of High-Speed Fiberoptic Systems", *Journal of Lightwave Technology*, vol. 14, no. 5, pp. 839-850, 1996

SFDR, OIP and Noise Level

In Chapter 2 the relation between $SFDR_n$, OIP_n and the noise floor is mathematically expressed in Equation (2.13). From the geometric point of view, $SFDR_n$ is $\frac{(n-1)}{n}$ times the distance between the noise floor and OIP_n . Figure A.1 shows this for two different noise levels, where the noise levels are denoted by $Noise_\alpha$ and $Noise_\beta$, respectively. In Figure A.1(a) the second-order intermodulation is considered. For both noise levels, $SFDR_2$ is $\frac{1}{2}$ times the corresponding distance between the noise floor and OIP_2 . In Figure A.1(b) the third-order intermodulation is considered. For both noise levels, $SFDR_3$ is $\frac{2}{3}$ times the corresponding distance between the noise floor and OIP_3 .

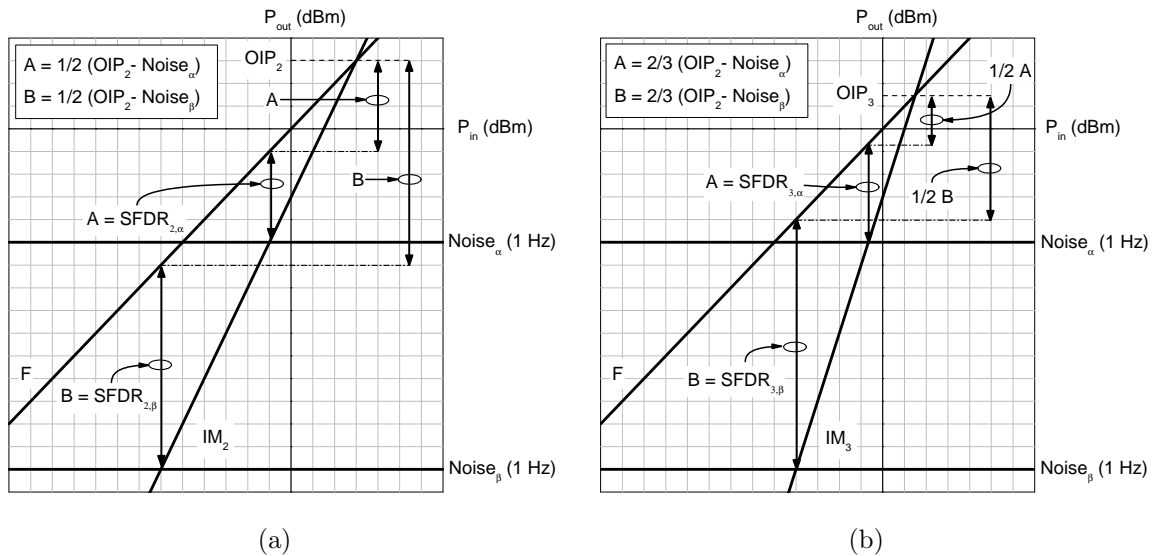


Figure A.1: Illustration of the relation between $SFDR_2$ and OIP_2 (a) and $SFDR_3$ and OIP_3 (b) for two different noise power levels.

Appendix B

Tables

Table B.1: Simulation parameters for the design of Figure 5.13 (three ring-resonators)

| Component | Parameter | Symbol | Value |
|-----------|-----------------------------------|--------------------------|------------|
| Ring A | ring power coupling coefficient 1 | $\kappa_{\text{ring},1}$ | 0.33 |
| | ring power coupling coefficient 2 | $\kappa_{\text{ring},2}$ | 0.33 |
| | ring round trip loss | l_{ring} | 0.175 (dB) |
| | ring free spectral range | FSR_{ring} | 0.50 |
| | ring round trip phase | ϕ_{ring} | 1.13 (rad) |
| Ring B | ring power coupling coefficient 1 | $\kappa_{\text{ring},1}$ | 0.33 |
| | ring power coupling coefficient 2 | $\kappa_{\text{ring},2}$ | 0.33 |
| | ring round trip loss | l_{ring} | 0.175 (dB) |
| | ring free spectral range | FSR_{ring} | 0.50 |
| | ring round trip phase | ϕ_{ring} | 0 |
| Ring C | ring power coupling coefficient 1 | $\kappa_{\text{ring},1}$ | 0.33 |
| | ring power coupling coefficient 2 | $\kappa_{\text{ring},2}$ | 0.33 |
| | ring round trip loss | l_{ring} | 0.175 (dB) |
| | ring free spectral range | FSR_{ring} | 0.50 |
| | ring round trip phase | ϕ_{ring} | 0 |

Table B.2: Simulation parameters for the design of Figure 5.16 (five ring-resonators)

| Component | Parameter | Symbol | Value |
|-----------|-----------------------------------|--------------------------|------------|
| Ring A | ring power coupling coefficient 1 | $\kappa_{\text{ring},1}$ | 0.33 |
| | ring power coupling coefficient 2 | $\kappa_{\text{ring},2}$ | 0.33 |
| | ring round trip loss | l_{ring} | 0.175 (dB) |
| | ring free spectral range | FSR_{ring} | 0.50 |
| | ring round trip phase | ϕ_{ring} | 1.13 (rad) |

Table B.3: Simulation parameters for the design of Figure 5.16 (five ring-resonators) [continued]

| Component | Parameter | Symbol | Value |
|-----------|-----------------------------------|--------------------------|-------------|
| Ring B | ring power coupling coefficient 1 | $\kappa_{\text{ring},1}$ | 0.33 |
| | ring power coupling coefficient 2 | $\kappa_{\text{ring},2}$ | 0.33 |
| | ring round trip loss | l_{ring} | 0.175 (dB) |
| | ring free spectral range | FSR_{ring} | 0.50 |
| | ring round trip phase | ϕ_{ring} | 0 |
| Ring C | ring power coupling coefficient 1 | $\kappa_{\text{ring},1}$ | 0.33 |
| | ring power coupling coefficient 2 | $\kappa_{\text{ring},2}$ | 0.33 |
| | ring round trip loss | l_{ring} | 0.349 (dB) |
| | ring free spectral range | FSR_{ring} | 0.25 |
| | ring round trip phase | ϕ_{ring} | 0.942 (rad) |
| Ring D | ring power coupling coefficient 1 | $\kappa_{\text{ring},1}$ | 0.33 |
| | ring power coupling coefficient 2 | $\kappa_{\text{ring},2}$ | 0.33 |
| | ring round trip loss | l_{ring} | 0.175 (dB) |
| | ring free spectral range | FSR_{ring} | 0.50 |
| | ring round trip phase | ϕ_{ring} | 0 |
| Ring E | ring power coupling coefficient 1 | $\kappa_{\text{ring},1}$ | 0.33 |
| | ring power coupling coefficient 2 | $\kappa_{\text{ring},2}$ | 0.33 |
| | ring round trip loss | l_{ring} | 0.349 (dB) |
| | ring free spectral range | FSR_{ring} | 0.25 |
| | ring round trip phase | ϕ_{ring} | 1.32 (rad) |